Hyperfine Interactions 123/124 (1999) 741–776

Backscattering mirrors for X-rays and Mössbauer radiation

Yu.V. Shvyd'ko and E. Gerdau

II. Institut für Experimentalphysik, Universität Hamburg, D-22761 Hamburg, Germany

Observation of exact backscattering of X-rays and studies of its energy and angular dependences; test of the validity of the dynamical theory of diffraction in the extreme case of exact backscattering; backscattering high-energy-resolution monochromators; backscattering interferometers, in particular of the Fabry–Pérot interferometer type; and precise, up to $5 \cdot 10^{-9}$ Å, measurements of crystal lattice parameters: these are central topics of the paper. Special attention is paid to the selection of crystals to be used as backscattering mirrors. Noncubic crystals like Al_2O_3, SiC, etc., allow backscattering for X-rays with practically any energy above 10 keV. Feasibility of backscattering mirrors for Mössbauer radiation of ^{57}Fe (14.4 keV), ^{151}Eu (21.5 keV), ^{119}Sn (23.9 keV), and ^{161}Dy (25.6 keV) nuclei is demonstrated by Al_2O_3 crystals. A concrete design of a sapphire Fabry–Pérot–Bragg étalon is presented.

Keywords: Bragg backscattering, X-rays, monochromators, interferometers, Al_2O_3, SiC

1. Introduction

The large coherence length of cm up to km of radiation from Mössbauer transitions is without precedent among all other sources in the hard X-ray region from 10 to 100 keV. This is a favourable starting condition for the successful demonstration of Fabry–Pérot, Michelson or other types of interferometers for radiation in this spectral range. Contrary to the visible spectral region where backscattering mirrors needed for an interferometric set-up are easy to produce, this is a central problem for hard X-rays.

The need for backscattering mirrors as components of X-ray resonators in different proposed schemes of γ-lasers or free electron X-ray lasers was expressed more than once in publications on these subjects.

Only recently X-rays were observed reflected from a crystal exactly opposite to the direction of the incident beam [1–3]. The observation of exact backscattering and studies of its properties are central topics of the present paper. The selection of crystals for backscattering mirrors, the use of Bragg mirrors in backscattering interferometers, resonators, and high-energy resolution monochromators for hard X-rays will be addressed as well.

Backscattering was first considered theoretically in the paper of Kohra and Matsushita [4]. Already in this publication two outstanding features were pointed out: approaching the Bragg angle of $\pi/2$ the reflection width reaches its smallest value on the energy scale and its largest value on the angular scale, see figure 1.

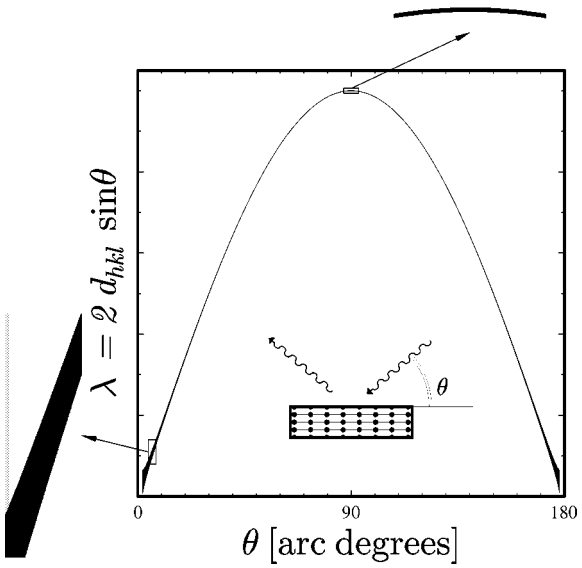

Figure 1. The solid line shows the region of high reflectivity of X-rays in a crystal for the case of two-beam Bragg diffraction; θ is the angle of incidence to the reflecting atomic planes (hkl) with interplanar distance d_{hkl} and λ is the wavelength of the X-rays. The curve is given by the kinematical Bragg law: $\lambda = 2d_{hkl}\sin\theta$. The width of the curve is defined in the dynamical theory of X-ray diffraction. The enlarged parts of the diagram display the advantages of backscattering: high reflectivity in a broad angular region with a narrow spectral width.

Backscattering was thus promising to found a basis of X-ray optics on with enhanced luminosity and high-energy resolution. These predictions have stimulated in the years following the publication [4] further theoretical [5–7] and experimental [7,8] studies of backscattering, as well as its application in different schemes of high-energy resolution monochromators and analyzers [9–16] for hard X-rays. Though restricted to angles of incidence deviating from normal incidence to the reflecting atomic planes by $\delta\theta \geqslant 2$ mrad the experiments of Graef and Materlik [7] and of Kushnir and Suvorov [8] have confirmed the two outstanding features of backscattering predicted by theory.

Woodruff et al. [17] have reported the first X-ray diffraction experiments at normal incidence to the reflecting planes. In an X-ray standing wave-field they observed emission of electrons and studied their energy profile. Cusatis et al. [1] were the first to observe X-rays reflected exactly backwards from a Si(1 1 1) plate at an energy of 1.9 keV. They studied the angular profiles in reflection and transmission. Soon afterwards we have reported the observation of exact backscattering and comprehensive studies of its energy and angular dependences in sapphire (Al_2O_3) single crystals with well collimated and ideally monochromatic 14.4 keV Mössbauer radiation [2]. A reflectivity of $\simeq$64% at exact backscattering close to the theoretical value of 88% was observed. A detailed comparison with the predictions of the dynamical theory of X-ray

diffraction was made. Kikuta et al. [3] have reported studies of the angular dependencies of transmissivity and reflectivity at a Bragg angle near $\pi/2$ in thin Si(9 9 1) crystal plates. In particular, they demonstrated that, approaching exact backscattering, the reflectivity drops drastically. This happens due to the transition of two-beam Bragg diffraction into multiple-beam diffraction while approaching normal incidence to the atomic planes in crystals with cubic symmetry. Soon after that Sinn et al. [18], using the set-up of [2], studied the effects of multiple-beam diffraction on the angular dependence of the reflectivity at normal incidence to atomic planes in Si crystals. Very recently Jach et al. [19] reported the observation of dynamical diffraction and X-ray standing waves at normal incidence to atomic planes in an AlPdMn quasi-crystal.

In the present paper we give more details of the experimental and theoretical studies of exact backscattering reported in [2], and discuss prospects of its applications in γ- and X-ray optics. In section 2 the selection of single crystals to be used as backscattering mirrors is addressed. In section 2.1 we show that perfect crystals of cubic type like Si are not optimal for this purpose. The arguments are supported by our recent measurements of the energy and angular dependences of the reflectivity in silicon at normal incidence to (12 4 0) atomic planes. In section 2.2 we extend the considerations to noncubic single crystals like sapphire, hexagonal or rhombohedral polytypes of silicon carbide (4H-SiC, 6H-SiC, 15R-SiC, etc.) and show that they are most appropriate for backscattering applications. Backscattering reflections in Al_2O_3 for X-rays matching selected Mössbauer transitions are given. In section 3 the experimental technique for the observation of exact backscattering is described. The results of studies of the reflectivity, the angular and energy profiles of backscattering by using 14.413 keV Mössbauer radiation of ^{57}Fe nuclei in sapphire crystals are given in section 3.2. In section 3.3 the experimental dependence of reflectivity is compared with that evaluated by the dynamical theory of diffraction, as outlined in the appendix. A systematic deviation from the exact line shape for backscattering predicted by the theory is pointed out. Application of backscattering for a very precise (up to $5\cdot10^{-9}$ Å) measurement of crystal lattice parameters is addressed in section 3.3.3. Results of tests of sapphire crystals as backscattering mirrors for Mössbauer radiation of other nuclei: ^{151}Eu (21.5 keV), ^{119}Sn (23.9 keV), and ^{161}Dy (25.6 keV) are presented in section 4. The performance of the sapphire mirror as part of a backscattering resonator is demonstrated in section 5. Design and simulations of a Fabry–Pérot–Bragg étalon for 14.413 keV Mössbauer radiation with sapphire single crystal plates as backscattering mirrors are presented in section 6.

In the appendix we recall elements of the dynamical theory of diffraction of X-rays in perfect crystals, laying emphasis on the points crucial in the backscattering geometry. Those equations are derived that are used in the present paper for the evaluation of angular, energy, and temperature dependences of the crystal reflectivity in backscattering as well as for the evaluation of the reflectivity and transmissivity of Fabry–Pérot–Bragg étalons.

2. Crystals for backscattering mirrors

Among commercially available single crystals those of Si have the highest quality. Their use in high resolution crystal X-ray optics is an established method. Despite this fact we decided to use Al_2O_3 (sapphire) and hexagonal or rhombohedral polytypes of silicon carbide (4H-SiC, 6H-SiC, 15R-SiC, etc.) single crystals as backscattering mirrors. There are several reasons for this choice.

2.1. Why not perfect Si?

Bragg's kinematical law

$$\lambda = 2d_{hkl}\sin\theta, \tag{2.1}$$

the relation between the wavelength λ of X-rays, their angle of incidence θ on the crystallographic planes (hkl) and the interplanar distance d_{hkl} reduces in the case of

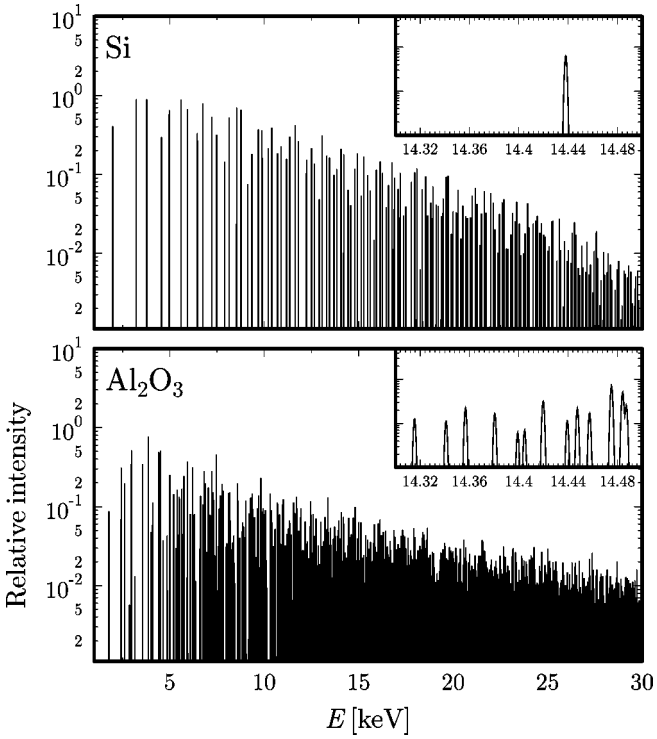

Figure 2. X-ray backscattering spectra of Si and Al_2O_3 single crystals calculated by the dynamical theory of diffraction for single crystal plates of 1 mm thickness. The positions of peaks in the spectra are defined by the Bragg energies eq. (2.2). The heights and widths of the peaks result from the convolution of the energy profile of the theoretical reflectivity curve with the energy profile of the incident radiation, which is assumed to be 2 eV broad. Peaks corresponding to n-times degenerate Bragg energies are taken to have n-times greater height. The insets show expanded spectra in the range 14.3–14.5 keV.

backscattering ($\theta = \pi/2$) to

$$\lambda = 2d_{hkl} \quad \text{or} \quad E = \frac{hc}{2d_{hkl}} \equiv E_{hkl}. \tag{2.2}$$

$E = hc/\lambda$ is the energy of the X-rays, and d_{hkl} is the interplanar distance. Thus, only for selected X-ray energies E_{hkl}, hereafter referred to as Bragg energies, back-reflections may occur in a given crystal.

In crystals with a cubic unit cell the interplanar distance is

$$d_{hkl} = a/\sqrt{h^2 + k^2 + l^2},$$

where a is the lattice constant. The same value of d_{hkl} and accordingly the same Bragg energy E_{hkl} belong to reflections with different Miller indices hkl. The Bragg energies in cubic crystals are therefore highly degenerate and the number of different Bragg energies is rather low: typically one per $\simeq$500–250 eV in the range 10–25 keV, see figure 2(Si). Tuning of a Bragg energy is equivalent to tuning of the lattice constant, which, for practical reasons, means a variation of the temperature. The temperature expansion coefficient in Si at room temperature is $a^{-1}\mathrm{d}a/\mathrm{d}T = 2.65 \cdot 10^{-6}$ K^{-1}. Thus, $\mathrm{d}E_{hkl}/\mathrm{dT} = 0.038$ eV/K for $E_{hkl} \simeq 15$ keV. I.e., to shift E_{hkl} by 100 eV, the temperature has to be changed by an unrealistic 2600 K. Therefore, Si single crystals allow backscattering only in limited regions of the X-ray spectrum. Unfortunately,

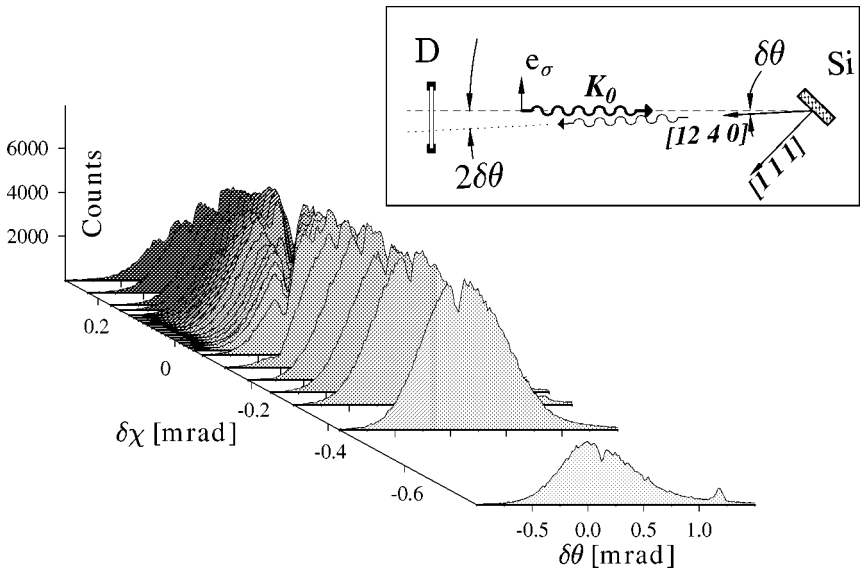

Figure 3. Two-dimensional angular dependence of the reflectivity of a Si single crystal for X-rays incoming close to normal incidence to the (12 4 0) atomic planes and the scheme of the experimental setup for its observation (in the inset). The angular divergence of the X-rays is $\simeq 20 \times 20$ μrad^2. $\delta\theta$ and $\delta\chi$ are deviations from normal incidence to (12 4 0) in the [1 1 1], [12 4 0] plane and in the plane perpendicular to it, respectively. The X-rays are monochromatized to an energy band of 7 meV width. The semitransparent detector D is placed at a distance of 0.8 m from the Si crystal.

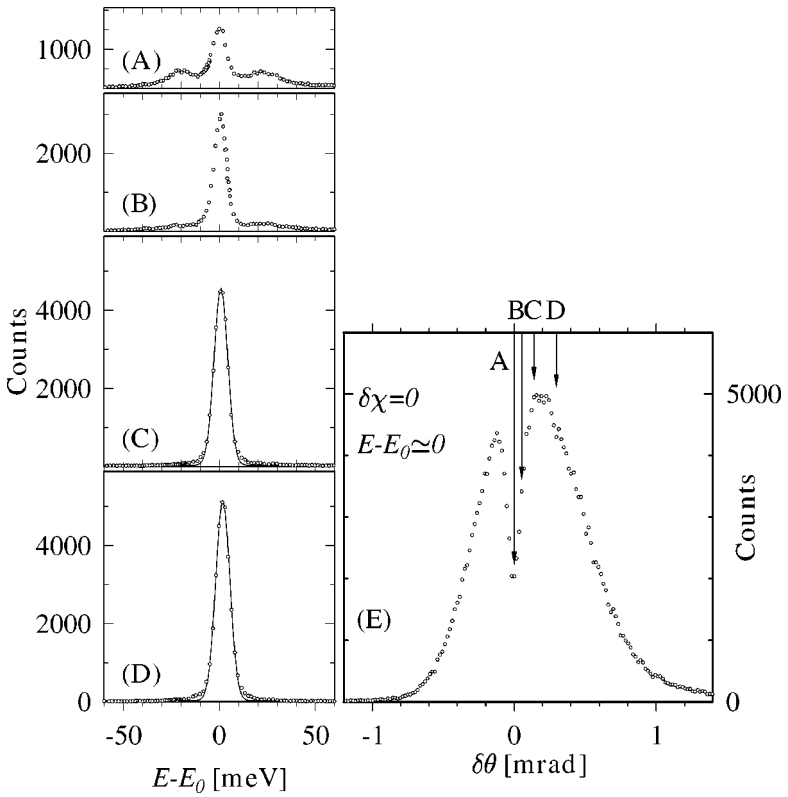

Figure 4. Energy (A), (B), (C), (D) and angular (E) dependences of the reflectivity of a Si single crystal for X-rays incoming close to normal incidence to the (12 4 0) atomic planes with $\delta\chi = 0$. A, B, C and D in (E) mark the $\delta\theta$ angular positions at which the energy spectra (A), (B), (C) and (D) are measured. The X-rays are monochromatized to an energy band of 7 meV width and scanned around $E_0 \simeq 14.438$ keV by using a high-energy resolution monochromator (figure 5(b)). The crystal temperature is $T \simeq 300$ K. Solid lines in (C) and (D) are fits with a Gaussian of 8.5 meV width.

there is no Mössbauer transition which by chance is close to a Bragg energy in Si that can be reached in the room temperature region. This imposes a first restriction on the use of Si crystals as backscattering mirrors.

Another restriction on using Si is due to multiple diffraction, which occurs in crystals with cubic symmetry at exact backscattering. The wave vector of the incident radiation fulfilling Bragg's conditions for backscattering for a certain reflection (hkl) points, in the reciprocal space of a crystal with cubic symmetry, always to an intersection of facets of one of its Brillouin zones. Thus, the condition for Bragg scattering is automatically fulfilled not only for the selected but also for other sets of atomic planes, namely for those parallel to the facets of the Brillouin zone. In crystals with cubic symmetry, exact backscattering co-exists with multiple diffraction.[1] For exam-

[1] The only exceptions to this rule are the very low-order Bragg reflections (1 1 1), (2 2 0). The reflection (1 1 1), corresponding to a Bragg energy of 1.9 keV, was applied in [1].

ple, 14.438 keV X-rays can be reflected backwards from the (12 4 0) atomic planes in Si at a temperature of $T \simeq 300$ K and at about 800 K it would reflect the 14.413 keV Mössbauer radiation of ^{57}Fe. However, at normal incidence an X-ray beam would simultaneously satisfy Bragg's conditions for another 22 allowed reflections among them: (0 2 2), (0 4 0), (4 2 6), (4 8 0), (6 0 6), (8 8 0), etc. Thus, approaching normal incidence to the (12 4 0) planes, new reflection channels for X-rays open up. One expects a reduced reflectivity in the backscattering channel and a complicated energy dependence. The results of our studies are shown in figures 3 and 4. The technique of backscattering measurements by using a semitransparent detector with a time resolution which allows observation of incident and reflected quanta separately is described in more detail in section 3.1. The two-dimensional angular dependence shown in figure 3 and a one-dimensional angular dependence measured at $\delta\chi = 0$ shown in figure 4 demonstrate that due to multiple-beam diffraction a dramatic decrease of the reflectivity of Si occurs while approaching normal incidence. The measured angular region of decreasing reflectivity is $\delta\theta \simeq \pm 0.2$ mrad. The energy dependence of the reflectivity 0.2 mrad off normal incidence shows a single peak, see figure 4(D). At normal incidence the spectrum changes drastically and shows a triple peak structure, see figure 4(A), which is due to multiple-beam diffraction. This very interesting mode of Bragg scattering deserves comprehensive experimental and theoretical studies on its own. However, they are beyond the scope of this paper.[2]

One more restriction on using Si crystals as backscattering mirrors is their low reflectivity for hard X-rays (a consequence of the relatively low Debye temperature). This is seen, e.g., from the rapid decrease of the backscattering spectrum in figure 2(Si) for $E \geqslant 25$ keV.

2.2. Non-cubic Al_2O_3, SiC, etc.

These problems can be avoided if one uses crystals (i) with lower crystal symmetry, (ii) with higher Debye temperature and (iii) with low photo-absorption. Hexagonal Al_2O_3, hexagonal and rhombohedral polytypes of silicon carbide (4H-SiC, 6H-SiC, 15R-SiC, etc.), BeO or Be are such crystals. In our experiments we have used commercially available high quality HEMEX sapphire (Al_2O_3) crystals, grown by the heat-exchange method [22].

The Bragg energies in Al_2O_3 are much less degenerate. Therefore, sapphire single crystals allow exact backscattering with a density of reflections of at least one per $\simeq$15 eV in the range 10–25 keV and even more for harder X-rays, see figure 2(Al_2O_3). By heating or cooling Al_2O_3 by no more than 100 K from room temperature one can fulfil the backscattering condition (2.2) for any X-ray energy above 10 keV. Table 1 illustrates this statement.

In table 1 we list Miller indices ($hkil$) of atomic planes (in the hexagonal basis, $h+k+i=0$) and the temperatures T_B of Al_2O_3 for which peak reflectivity at normal

[2] Comprehensive studies of the Si(12 4 0) backscattering case are presented in [21], theoretical studies of the Si(9 9 1) backscattering case are presented in [20].

Table 1
Miller indices ($hkil$) of atomic planes (in the hexagonal basis, $h+k+i=0$) and Bragg temperatures $T_{\rm B}$ of Al_2O_3 for which the peak reflectivity at normal incidence occurs at X-ray energies E matching selected Mössbauer transitions. Other symbols are explained in the text.

Nucleus	E keV	$(hkil)$ hexagonal	$T_{\rm B}$ K	$\Delta\theta$ μrad	ΔE meV	Reflectivity	Extinction (mm)	$\mathrm{d}E/\mathrm{d}T$ eV/K
^{181}Ta	6.2155	$(1\,\bar{3}\,2\,10)$	251.1	3373.5	58.340	0.888	0.004	−0.038
^{73}Ge	13.263	$(2\,6\,\bar{8}\,\bar{16})$	320.5	1246.7	9.458	0.900	0.022	−0.093
^{57}Fe	14.4125	$(1\,3\,\bar{4}\,28)$	379.5	1009.5	6.156	0.879	0.034	−0.098
^{151}Eu	21.5415	$(11\,2\,\bar{13}\,24)$	254.5	525.6	2.615	0.917	0.081	−0.145
^{149}Sm	22.494	$(3\,13\,\bar{16}\,8)$	241.5	569.8	2.362	0.912	0.089	−0.164
^{119}Sn	23.8795	$(9\,1\,\bar{10}\,\bar{40})$	297.0	444.1	1.779	0.908	0.119	−0.151
^{161}Dy	25.6513	$(5\,10\,\bar{15}\,34)$	421.5	403.1	1.613	0.919	0.131	−0.191
^{129}I	27.77	$(7\,13\,\bar{20}\,\bar{18})$	447.5	363.6	1.144	0.907	0.185	−0.213
^{40}K	29.56	$(16\,5\,\bar{21}\,\bar{16})$	396.5	283.7	0.733	0.882	0.287	−0.223
^{201}Hg	32.19	$(5\,18\,\bar{23}\,14)$	407.5	242.9	0.597	0.889	0.354	−0.244
^{125}Te	35.46	$(3\,13\,\bar{16}\,\bar{58})$	290.5	213.9	0.489	0.899	0.433	−0.224
^{189}Os	36.22	$(7\,8\,\bar{15}\,\bar{64})$	461.5	181.2	0.351	0.870	0.603	−0.278
^{121}Sb	37.15	$(16\,12\,\bar{28}\,\bar{14})$	486.5	157.1	0.263	0.842	0.806	−0.288
^{129}Xe	39.58	$(21\,8\,\bar{29}\,\bar{14})$	331.5	132.3	0.194	0.825	1.095	−0.295
^{161}Dy	43.83	$(12\,19\,\bar{31}\,\bar{34})$	322.5	092.4	0.101	0.766	2.111	−0.319
^{238}U	44.915	$(15\,19\,\bar{34}\,14)$	230.5	79.8	0.076	0.720	2.808	−0.327
^{183}W	46.4837	$(17\,17\,\bar{34}\,\bar{30})$	476.5	63.6	0.049	0.636	4.350	−0.360
^{127}I	57.60	$(20\,24\,\bar{44}\,\bar{10})$	284.5	23.4	0.008	0.205	33.294	−0.428

incidence occurs at X-ray energies matching selected Mössbauer transitions. In the present paper $T_{\rm B}$ is referred to as Bragg temperature, which applies to a selected set of atomic planes (hkl) and to a selected X-ray energy.

Generally there exists more than one set of reflecting atomic planes for each X-ray energy. Data for only one set with the highest reflectivity and with the Bragg temperature in the range $200 \leqslant T_{\rm B} \leqslant 500$ K are given. The table provides for each reflection the calculated angular width $\Delta\theta$, the energy bandpass ΔE, the maximum reflectivity, the extinction length $L_{\rm ext} = \lambda/(2\pi|\chi_H|)$, and the variation of the energy at the position of peak reflectivity with crystal temperature $\mathrm{d}E/\mathrm{d}T$. All calculations were performed with the dynamical theory of X-ray diffraction in perfect crystals, outlined in the appendix. The crystals are assumed to be semi-infinite.

According to this table, for X-rays matching the 14.4125 keV Mössbauer transition in ^{57}Fe nuclei, a $(1\,3\,\bar{4}\,28)$ back reflection can be predicted at $T_{\rm B} = 380$ K in sapphire with an angular acceptance of 1.0 mrad, an energy bandwidth of 6.2 meV, and 88% reflectivity.

It is remarkable that even for X-rays with relatively high energy, e.g., for those matching the 57.6 keV Mössbauer transition in ^{127}I, sapphire offers reflections with high reflectivity, with an angular acceptance large enough to fit the divergence of radiation from present day undulator based X-ray sources, and with an energy bandpass

as low as 8 μeV. However, for this to be realized, a more than 3 cm thick perfect sapphire crystal has to be used that must be kept in an environment with a temperature stability better than 10 μK.

The crystallographic data used in the evaluations are taken from [23]. The thermal expansion data are taken from [24]. It should be noted that lattice constants and thermal expansion data for Al_2O_3 reported by different authors [23,25–28] differ by 100 ppm. This imposes an uncertainty on the predicted Bragg temperatures. We estimate that the Bragg temperatures given in the table may deviate from their real values by ± 15 K. In section 4 measured Bragg temperatures for selected X-ray energies will be given. We also report there lattice parameters of Al_2O_3 at two temperatures, derived from our data.

3. Exact backscattering

3.1. Experimental method

The observation of exact 180°-scattering has an obvious experimental difficulty. Either the X-ray source or the detector is blocking the reflected or the incident X-rays. There are only two possibilities to overcome this problem.

One is to use a transparent X-ray source, wiggler or undulator, as proposed in [7, 9,29,30]. The construction of such an exact backscattering beam-line was announced at the APS (Argonne) [30].

Another possible way, which was realized in [1], is to use a semi-transparent detector. However, in this case the reflected radiation is observed on the strong background of the incident radiation.

To discriminate against this background we proposed to insert a semi-transparent detector with a good time resolution and make use of the pulsed structure of synchrotron radiation [2]. The time-of-flight $\tau = 2L/c$ to the crystal and back to the detector separated by a distance L allowed us to distinguish between the incident and reflected radiation pulses, see figures 5 and 6.

The experiments further described in this paper were performed mostly at the wiggler beam line BW4 at HASYLAB, Hamburg ($L = 9.9$ m and $\tau = 66$ ns). The DORIS-III positron storage ring was operated in the five-bunch mode, producing synchrotron radiation pulses from the wiggler every 192 ns ($\sim$200 ps duration). A high-heat-load Si(1 1 1) monochromator (M) provided 14.413 keV radiation with $\simeq$3 eV bandwidth. The beam divergence was typically 20 μrad in the vertical and 80 μrad in the horizontal plane, i.e., much less than the angular acceptances of back reflections in Al_2O_3 in this energy range (see table 1).

To study the properties of backscattering one not only needs collimated but also monochromatic radiation. We used 14.413 keV Mössbauer radiation of ^{57}Fe nuclei for this purpose. The energy spectrum of the Mössbauer radiation, even for the largest observed broadening, is within a band of 1 μeV width, which can be considered as quasi mono-energetic relative to the energy widths of backscattering reflections of

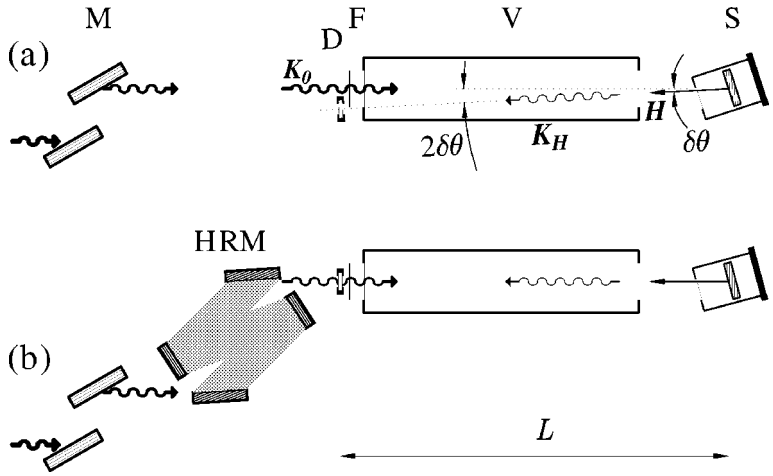

Figure 5. Set-ups for backscattering experiments. (a) M is the Si(1 1 1) high-heat-load monochromator; D is a semi-transparent X-ray detector; F is a 10 μm thick ^{57}Fe foil; V is a vacuum tube of 1–10 m length; S is a backscattering single crystal in an oven; $\delta\theta$ is the angle between the wave vector $\boldsymbol{K}_0$ of the incident radiation and the scattering vector $\boldsymbol{H}$; $\boldsymbol{K}_H = \boldsymbol{K}_0 + \boldsymbol{H}$ is the wave vector of the scattered radiation. (b) The high-energy resolution monochromator (HRM) monochromatizes the incident radiation to a meV bandwidth.

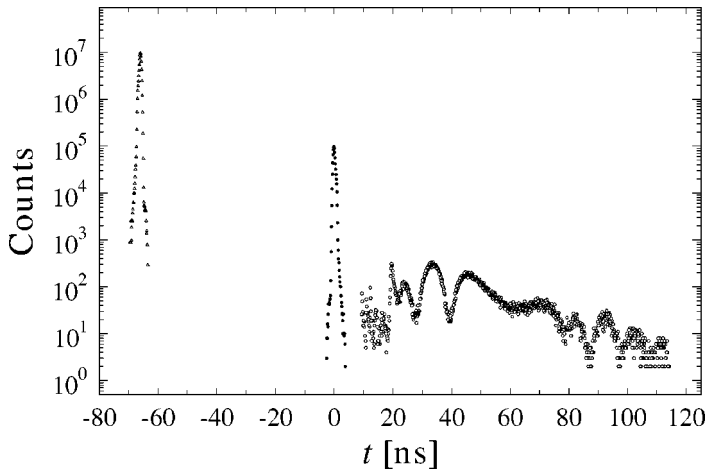

Figure 6. Counts in the semi-transparent detector as seen on the time scale. The detector is placed at a distance of $L \simeq 9.9$ m from the reflecting crystal. At $t \simeq -66$ ns: primary radiation pulse; at $t \simeq 0$: back reflected radiation pulse; at $t > 0$: back reflected resonant radiation.

typically $\leqslant$10 meV. A collimated beam of Mössbauer photons is generated by spatially coherent excitation of the 14.4 keV resonance in ^{57}Fe nuclei in a 10 μm thick iron foil (F in figure 5) with synchrotron radiation pulses. The iron foil was enriched in ^{57}Fe to 95%. Due to coherent enhancement the ensemble of excited ^{57}Fe nuclei emits

photons in the direction of the incident beam (see [31] and references therein) with a delay of ≈20–50 ns. The time spectrum of the radiation scattered in the forward direction is shown in figure 6.

An avalanche photodiode EG&G C30703F with a 100 μm thick sensitive Si wafer serves as the semi-transparent detector.[3] The transverse size of the diode is 15×15 mm^2 with a sensitive area of 10×10 mm^2. Its time resolution is 1 ns [32] and allows one to distinguish between the incident pulse and the pulse reflected from a crystal at $L \geqslant 0.5$ m distance. This time resolution is used twice in the experiment. First, to distinguish between the incident and the reflected radiation pulses. Second, to count only 14.413 keV photons from the 0.5 μeV energy band, scattered by ^{57}Fe nuclei in the forward direction.

The diode in combination with the timing electronics is able to detect a photon flux up to $\simeq 10^8$ Hz. The flux after the high-heat-load monochromator is significantly larger. Therefore, to observe exact backscattering, either an absorber or a high-energy resolution monochromator[4] (see figure 6(b)) is installed. The latter reduces the energy band of the incident beam from ≃2 eV to ≃7 meV and correspondingly the total flux, preserving the flux of "good" photons. Depending on the situation we use one of these methods. Sometimes we also use a third set-up. However, the diode is then put as close as possible to the incident beam, see figure 6(a). The deviation from exact backscattering in our geometrical arrangement can be chosen as small as 0.2 mrad, which in the cases discussed in the present section is almost equivalent to exact backscattering since the widths of the measured angular dependences are typically 1 mrad.

For studies of exact backscattering the $(1\,3\,\bar{4}\,28)$ atomic planes in Al_2O_3 were chosen, as backscattering of the 14.413 keV Mössbauer radiation is predicted for this set of planes at a moderate temperature of 380 K (see table 1).

In the experiments, sapphire crystals in the form of a disk of 15 mm diameter and 1 mm thickness cut perpendicular to the axis [0 0 0 1] were employed.[5] They were installed in an oven on a four-circle diffractometer at the end of the vacuum tube, see figure 5.

Backscattering of the 14.413 keV Mössbauer radiation from the $(1\,3\,\bar{4}\,28)$ atomic planes is searched for as follows. First the crystal axis [0 0 0 1] is oriented parallel to the incident beam by detecting exact back reflection (0 0 0 30) of X-rays with energy $E = 14.317$ keV (crystal at room temperature). All photons are counted except those incident at $t \simeq -66$ ns. Then the atomic planes $(1\,3\,\bar{4}\,28)$ are set perpendicular to the incident beam by detecting exact back reflection of the incident 14.413 keV

[3] We are indebted to Dr. Henri Dautet from the EG&G Optoelectronics Ltd., Vaudreuil, Quebec, for delivering photodiodes without a ceramic stiffener in the back and without a back-cover.

[4] The high-energy resolution monochromator used in the experiments at HASYLAB built with channel-cut Si(4 2 2) and Si(12 2 2) crystals in nested geometry was designed by E. Gerdau, R. Rüffer and H.D. Rüter based on the initial proposal of [12].

[5] The crystals were obtained from ESCETE B.V. Single Crystal Technology, Schiffstraat 220, NL-7574 RD Enschede, the Netherlands.

photons.[6] The angular position of the crystal at which it reflects these X-rays back into the detector with maximum intensity is taken as the reference point $\delta\theta = 0$ for exact backscattering. At this stage of the adjustment procedure the Mössbauer photons generated in the iron foil do not necessarily fall into the energy band of the (1 3 $\bar{4}$ 28) back reflection. As a next step the temperature of the crystal is scanned until events within a time window of 20–120 ns are detected (figure 6). This signals that the crystal reflects Mössbauer photons backwards.

3.1.1. T–E equivalence relation

Being bound to the fixed energy of the Mössbauer radiation, the standard measurement of the reflectivity as a function of the X-ray energy E is replaced by the equivalent reflectivity measurement as a function of the crystal temperature T.

The T–E equivalence relation can be derived easily. As discussed in the appendix, according to the dynamical theory of diffraction the reflectivity is a function of the deviation from Bragg's condition given by the parameter α, which is a function of T and E. Those values of E and T are equivalent which result in the same value of α. Using the general expression (A.11) for α, derived in the appendix without approximations, and the definition of the Bragg energy (2.2) one finds that α is a function of the product $Ed_{hkl}(T)$. Therefore, the condition for the E–T equivalence reads $Ed_{hkl}(T) = \text{const}$, or, after differentiation,

$$\frac{\mathrm{d}E}{\mathrm{d}T} = \frac{E_{hkl}}{d_{hkl}} \frac{\mathrm{d}d_{hkl}}{\mathrm{d}T}. \tag{3.1}$$

For more details see appendix A.2.

By using the temperature expansion in the [1 3 $\bar{4}$ 28] direction derived in equation (3.6), we obtain for X-rays with energy $E \simeq 14.413$ keV and for a crystal temperature $T \simeq 372$ K

$$\frac{\mathrm{d}E}{\mathrm{d}T} = -0.100 \text{ [eV/K]} \tag{3.2}$$

in the case of Bragg scattering from the atomic planes (1 3 $\bar{4}$ 28).

3.2. Studies of exact backscattering in the two-beam diffraction case

3.2.1. Temperature dependences

Figure 7 shows temperature dependences of the reflectivity recorded at different angular deviations $\delta\theta$ from normal incidence to the (1 3 $\bar{4}$ 28) planes. The temperature in the oven was stabilized with an accuracy of 1 mK by using computer control [33]. A platinum resistor PT100 was used as a temperature sensor.

[6] The angle ψ between the [0 0 0 1] and [1 3 $\bar{4}$ 28] directions is 22.091°. There are another 5 reciprocal vectors equivalent to [1 3 $\bar{4}$ 28]. They lie on the surface of a cone with opening angle ψ and rotation axis parallel to [0 0 0 1]. Back reflections corresponding to these reciprocal vectors are easily found by directing the incident beam at an angle of ψ to the [0 0 0 1] axis and by rotating the crystal around the [0 0 0 1] direction.

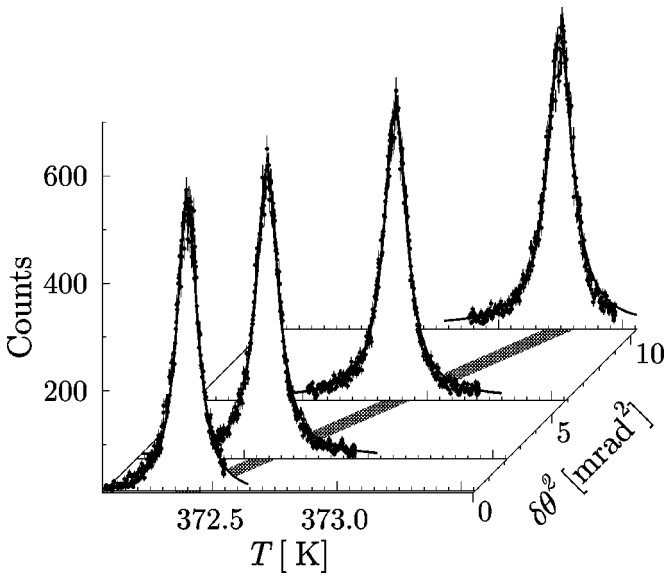

Figure 7. Temperature dependences of Bragg scattering of 14.413 keV photons with 0.5 μeV bandwidth from an Al_2O_3 crystal measured at different angular deviations $\delta\theta$ from normal incidence to the $(1\,3\,\bar{4}\,28)$ reflecting planes. Solid lines are fits with Lorentzians. The width of the curve at $\delta\theta = 0.2$ mrad is 100 mK (equivalent to a 10.0 meV X-ray energy bandwidth).

At $\delta\theta = 0.2$ mrad (i.e., in almost exact backscattering) the maximum reflectivity is achieved in this sample at $T_B = 372.40 \pm 0.01$ K. The width of the reflection curve is 100 mK, corresponding to an energy width of 10.0 meV. This is more than the 6.2 meV expected theoretically. With increasing $\delta\theta$ the temperature where maximum reflectivity is reached increases proportional to $\delta\theta^2$. This square dependence, which is a characteristic feature of backscattering, has a remarkable consequence, namely an extraordinarily large angular acceptance of Bragg back reflections. The corresponding measurements are shown below in section 3.2.2.

The temperature dependence of almost exact backscattering was measured in sapphire single crystals of different origin. The width and the form of the temperature dependence served as a crystal quality test. Czochralski grown crystals[7] show energy widths of typically about 40–50 meV. HEMEX sapphire [22] shows significantly narrower reflection curves with widths from 20 meV down to the theoretical value of 6.2 meV, see figure 8. All samples were mechanically polished as described in [22].

To reduce possible tension in a surface layer due to mechanical polishing, some samples were chemically polished in a 1 : 1 H_2SO_4 : H_3PO_4 solution, as described in [34]. The effect of chemical polishing, although not very pronounced, was positive. The narrowest temperature dependence, shown in figure 8, was measured in a crystal

[7] The samples were obtained from Union Carbide via Roditi International Corporation GmbH, D-21029 Hamburg, Germany.

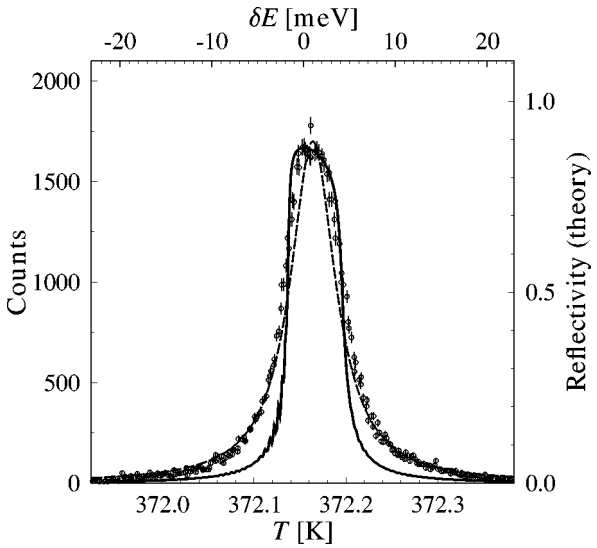

Figure 8. Reflectivity in Al_2O_3 (circles) measured at almost exact backscattering with $\delta\theta = 0.2$ mrad as a function of the crystal temperature T [35]. The upper scale is in units of the X-ray energy equivalent to the temperature change. The solid line is the calculation according to the dynamical theory for an ideal 1 mm thick crystal of Al_2O_3 and an incident monochromatic plane wave, see eqs. (A.31), (A.27), (A.21) and (A.11) of the appendix. The dashed line is a Lorentzian with a width of 6.2 meV.

polished in the above solution for 6 hours at $300 \pm 10^{\circ}$C. A surface layer of $\simeq$0.15 mm is removed by this procedure.

T_B differs slightly from sample to sample. Its average value, calculated from the data of about 30 measured samples of HEMEX sapphire, is $\langle T_B \rangle = 372.19$ K with a mean square deviation of ± 0.06 K.

3.2.2. Angular dependences

Figure 9 shows the angular dependences of Bragg scattering of 14.413 keV resonant radiation measured at different temperatures T of the same Al_2O_3 crystal. The angle $\delta\theta$ of deviation from exact backscattering was varied only in one direction. Because of the symmetry of scattering at 90° this is equivalent to a variation in the opposite direction. Therefore, the angular dependences of figure 9 are symmetric with respect to $\delta\theta = 0$.

Below T_B, i.e., at $T - T_B = \Delta T < 0$, Bragg scattering scarcely takes place. Approaching T_B Bragg scattering builds up, with its maximum of reflectivity at $\delta\theta = 0$ and the largest angular width (full width at half maximum) of 1.7 mrad at $\Delta T = 0$. With a further increase of temperature the peak reflectivity is shifted to values of $\delta\theta \neq 0$, the rocking curve narrows and gradually acquires the form known in conventional Bragg scattering. Nevertheless, the width of the Bragg reflection at $\delta\theta = 2.78$ mrad still has the extraordinarily large value of 0.24 mrad.

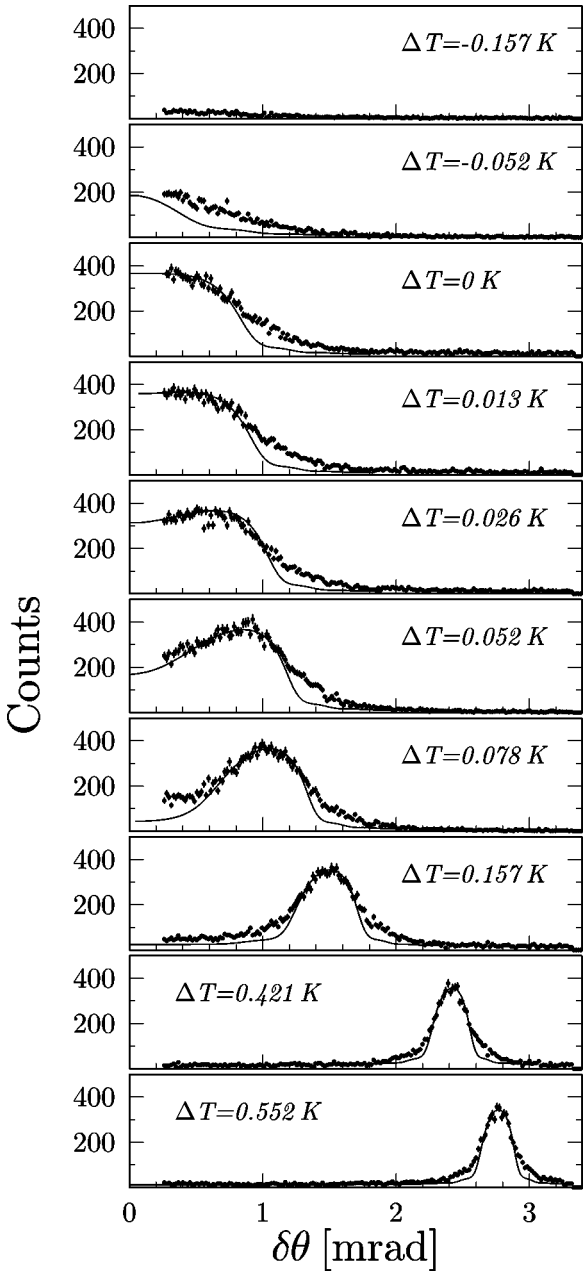

Figure 9. The angular dependences of Bragg scattering of monochromatic 14.413 keV X-rays with 0.5 μeV bandwidth measured at different temperatures T of an Al_2O_3 crystal utilizing the $(1\,3\,\bar{4}\,28)$ reflection. $\delta\theta$ is the angular deviation from normal incidence of the X-rays to the $(1\,3\,\bar{4}\,28)$ reflecting planes. $\Delta T = T - T_B$, where $T_B = 372.40$ K. Solid lines are fits using the dynamical theory of Bragg scattering.

3.2.3. Peak reflectivity at normal incidence

The peak reflectivity is constant at different deviations $\delta\theta$ from normal incidence. To measure the absolute value of the peak reflectivity at normal incidence to $(1\,3\,\bar{4}\,28)$ planes in Al_2O_3 a high-energy resolution monochromator was installed, see figure 5(b). This reduces the flux without loss of "good" photons to such an amount that the full incident beam does not damage the semi-transparent detector. The iron foil in these measurements is put in front of the detector. Now the time spectrum of nuclear forward scattering from the iron foil appears twice in the detector with a $2L/c$ separation in time: once direct from the foil beginning at $t > -66$ ns and for the second time at $t > 0$ ns reflected from the sapphire crystal. The ratio of the time integrated count rates of both time spectra gives the reflectivity of sapphire multiplied by the transmissivity of the detector. The transmissivity is easily measurable. The reflectivity of the sapphire crystal for the 14.413 keV nuclear resonant radiation is found to be 64%. This value applies to the sample used in the measurements shown in figures 7 and 9. It is remarkable that the measured reflectivity, even for a not perfect crystal, is close to the value of 88% calculated for perfect crystals.

3.3. Evaluation of data and discussion

The experimental data can be compared with the predictions of the dynamical theory of backscattering of X-rays outlined in the appendix.

The main predictions of the theory are summarized graphically in figure 10. The ordinate of the graph is $(E - E_{hkl})/E_{hkl}$ – the deviation of the X-ray energy E from the Bragg energy E_{hkl} expressed in units of E_{hkl}. The abscissa is the square of the angular deviation from normal incidence, $\delta\theta^2$. The spectral-angular region of total reflection for a perfect non-absorbing crystal – a kind of DuMond diagram – is given in this representation by the straight grey strip, according to eqs. (A.18), (A.36) of the appendix. The width of the grey strip along both axes scales with the value of

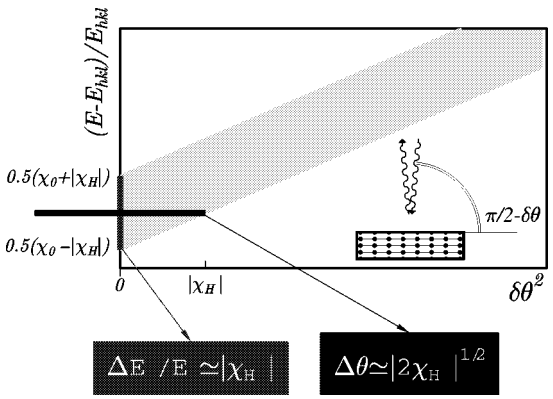

Figure 10. Spectral-angular region of total reflection of backscattering. Note that the abscissa scales with $\delta\theta^2$.

χ_H – the Fourier component of the electric susceptibility, see eqs. (A.1), (A.2) of the appendix. Typically $|\chi_H| \simeq 10^{-6}$–10^{-7} for 15 keV X-rays.

At normal incidence ($\delta\theta = 0$) X-rays which are reflected backwards are centered around an energy $E = E_{hkl}(1 - \chi_0/2)$ slightly larger than E_{hkl}. As discussed in the appendix, eq. (A.35), this is due to refraction in the crystal which scales with $\chi_0 \approx -10^{-5}$. The relative width of the region on the energy scale is $\Delta E/E \simeq \chi_H$ and equivalently $\Delta T/T \simeq \chi_H$.

An important feature of the DuMond diagram for backscattering is that the angular scale – the abscissa – has a $\delta\theta^2$ dependence, resulting in an unusually large width of the angular region of total reflection of $\Delta\theta \simeq \sqrt{2\chi_H}$.

The diagram helps to see that the sets of measured temperature and angular profiles of backscattering shown in figures 7 and 9 qualitatively agree with the theoretical predictions, but not in details.

3.3.1. Temperature dependences

Practically for all measured samples the temperature dependences of backscattering can be fitted by Lorentzian curves (cf. figure 7) having a width larger than predicted for a perfect crystal. This is an unusual line form, which differs significantly from the Darwin–Prins curve predicted by the dynamical theory of diffraction in perfect crystals. Further, the Lorentzian distribution which we observe can not be caused by an energy or angular distribution of the incident beam, as our measurements were performed with ideal monochromatic and well collimated X-rays.

The only measured exception is in the temperature dependence shown in figure 8. The width and the central part of the experimental curve fit well to the theoretical Darwin–Prins curve calculated with the theory of dynamical diffraction extended to backscattering as outlined in the appendix. However, the wings again fit better to a Lorentzian. Most probably, the Lorentzian line shape is a result of crystal imperfections. The challenge to account for the observed Lorentzian distribution remains.

3.3.2. Angular dependences

The angular dependences shown in figure 9 were compared with the dependences calculated by the dynamical theory extended to the case of backscattering. We made certain assumptions to account for the observed broadening of the temperature and angular curves. As the type of crystal defects causing the broadening was not known, it was assumed that the defects subdivide the crystal into perfect blocks of finite thickness. The thinner the block, the broader the reflectivity curve. We have ascertained that the calculated angular dependences averaged over block thicknesses in the range $\ell = 70 \pm 70$ μm may satisfactorily describe our experimental results, as shown by solid lines in figure 9. Still, the fit is not ideal and the wings of the experimental dependences are decaying slower than the theoretical curves.

The following data were used in the calculations: $E = 14.413$ keV, $\chi_0 = (-78.4 + \mathrm{i}\,0.29) \times 10^{-7}$, $\chi_H = (-4.04 + \mathrm{i}\,0.13) \times 10^{-7}$, $b = -1$.

3.3.3. Crystal lattice parameters

The backscattering geometry is especially favourable for a precise determination of lattice parameters of the reflecting crystal. One of the techniques based on Bragg backscattering at fixed wavelength (energy) of the incident radiation is presented here.

For backscattering Bragg's law reads

$$\lambda = 2d_{hkl}(T+\Delta T)\sin\left(\frac{\pi}{2}-\delta\theta\right) \simeq 2d_{hkl}(T+\Delta T)\left(1-\frac{1}{2}\delta\theta^2\right). \qquad (3.3)$$

More precisely, taking into account refraction and assuming low photoabsorption in the crystal ($\chi_0'' \ll |\chi_0'|$), one gets, in the frame of the dynamical theory,

$$\tilde{\lambda} = \lambda\left(1-\frac{\chi_0'}{2}\right) = 2d_{hkl}(T+\Delta T)\left(1-\frac{\delta\theta^2}{2}\right). \qquad (3.4)$$

Here $\chi_0' = \mathrm{Re}\{\chi_0\} < 0$ and $\chi_0'' = \mathrm{Im}\{\chi_0\}$. $\tilde{\lambda}$ is the wavelength of the radiation in the crystal. It is exactly backscattered at the temperature T. Equation (3.4) can be rewritten, using $d_{hkl}(T+\Delta T) = \tilde{\lambda}/2 + \Delta d_{hkl}$, as

$$\Delta d_{hkl} = \frac{\tilde{\lambda}}{4}\delta\theta^2. \qquad (3.5)$$

According to eq. (3.5) Δd_{hkl} depends on the square of the angular position $\delta\theta$ of maximal reflectivity. This is a special property of backscattering, which therefore is extremely sensitive to tiny changes of the lattice constant. If $\delta\theta$ can be measured with an accuracy of 0.1 mrad, $\Delta d_{hkl} \approx 10^{-9}\tilde{\lambda}$. Indeed, the fit of the curves shown in figure 9 turned out to be sensitive to variations of the average interplanar distance as $\Delta d_{hkl} \simeq 5\times10^{-9}$ Å.

As $\tilde{\lambda}$ is defined by the extreme sharpness of the Mössbauer radiation, this method opens the possibility of very precise measurements of the average crystal lattice parameters in units of the Mössbauer wavelength λ. We estimate the accuracy to be better than $10^{-8}\lambda$. The precision is limited mostly by the accuracy of χ_0.

The values of $\delta_{[1\,3\,\bar{4}\,28]} = 2d_{[1\,3\,\bar{4}\,28]}/\tilde{\lambda} - 1$ and of $d_{[1\,3\,\bar{4}\,28]}$ at different temperatures (above T_B) obtained from the fits of the measured angular dependences of figure 9 are shown in figure 11. The set of points in figure 11 can be approximated by a linear temperature dependence:

$$d_{[1\,3\,\bar{4}\,28]}(T) = \frac{\tilde{\lambda}}{2}\left[1+6.944\times10^{-6}(T-T_\mathrm{B})\right], \quad T_\mathrm{B} = 372.40\ \mathrm{K}. \qquad (3.6)$$

In standard length units the value for the wavelength of the Mössbauer radiation in sapphire is $\tilde{\lambda} = 0.8602583$ Å. It is derived from the vacuum value $\lambda = 0.8602549(12)$ Å [36] ($E = 14412.50(2)$ eV) and $\chi_0' = -0.784\times10^{-5}$.

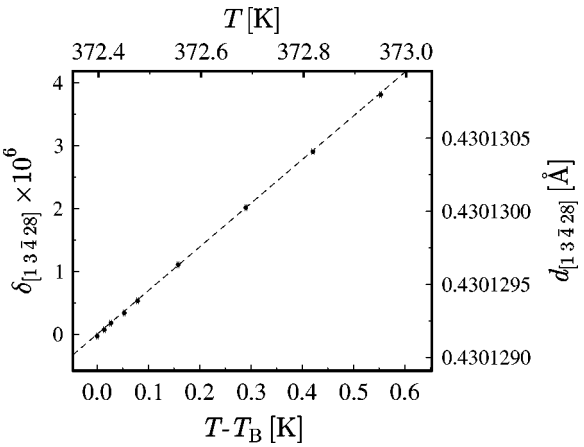

Figure 11. Temperature variation of the relative interplanar distance $\delta_{[1\,3\,\bar{4}\,28]}$ in Al_2O_3 measured in units of the half Mössbauer wavelength $\tilde{\lambda}/2$ in sapphire: $\delta_{[1\,3\,\bar{4}\,28]} = d_{[1\,3\,\bar{4}\,28]}/(\tilde{\lambda}/2) - 1$. The data are derived from the fit of the angular dependences of backscattering (figure 9) measured at fixed values of the crystal temperature T. The absolute values of $d_{[1\,3\,\bar{4}\,28]}$ are given taking $\tilde{\lambda} = 0.8602583$ Å (see text). The dashed line is a linear fit using eq. (3.6).

4. Sapphire as a universal backscattering mirror

As shown in section 2.2 (see especially figure 2 and table 1), in noncubic crystals like sapphire the number of different Bragg energies per energy interval is sufficiently large to find at any γ-energy of about 10–50 keV a backscattering reflection by a moderate change of the temperature. Along with 14.4125 keV Mössbauer radiation of ^{57}Fe nuclei, almost exact backscattering was also observed for the 21.5415 keV Mössbauer radiation of ^{151}Eu [37], the 23.8795 keV radiation of ^{119}Sn [37], and for the 25.6513 keV radiation of ^{161}Dy [38].

In table 2 we summarize measured Bragg temperatures, as well as temperature and energy width of the observed back reflections. The experiments were performed at the undulator beamlines at APS (SRI-CAT 3ID) [37] and HASYLAB (PETRA1) [38] by using set-ups very similar to that shown in figure 5(a). Details of the experimental results are given in [37,38].

All observed reflections have a narrow energy width. However, the measured energy widths are larger than the predicted values given in braces. Again the most probable reason for this is an insufficient crystal perfection.

The measured Bragg temperatures systematically deviate by $\simeq$10 K from the Bragg temperatures calculated by using the lattice constants determined in [23,24] – table 1.

The lucky coincidence of the Bragg temperatures for ^{151}Eu and ^{119}Sn Mössbauer radiation allowed us to determine more accurately the lattice constant in HEMEX sapphire at $T_B = 287.35$ K via the known energies of the Mössbauer lines:

$$a = 4.7590(4)\ \text{Å}, \quad c = 12.99085(22)\ \text{Å} \quad \text{at} \quad T = 287.35\ \text{K}.$$

Table 2
Atomic planes ($hkil$) and Bragg temperatures T_B of Al_2O_3 for which peak reflectivity in almost exact backscattering geometry ($\delta\theta = 0$) occurs at X-ray energies E matching selected Mössbauer transitions. Rated values of the energy widths and peak reflectivities are added in braces. Experimental errors are given in parentheses.

Nucleus	E keV	$(hkil)$ hexagonal	T_B K	ΔT mK	ΔE meV	Reflectivity
^{57}Fe	14.41250(2) [36]	$(1\,3\,\bar{4}\,28)$	372.19(6)	62	6.2 {6.2}	0.80 {0.88}
^{151}Eu	21.54149(16) [39]	$(3\,2\,\bar{5}\,43)$	287.34(15)	69	8.7 {0.6}	– {0.65}
^{119}Sn	23.8795(5) [40]	$(1\,9\,\overline{10}\,40)$	287.35(15)	77	11.5 {1.7}	– {0.91}
^{161}Dy	25.65129(16) [39]	$(3\,2\,\bar{5}\,52)$	375.11(15)	46	8.0 {0.8}	– {0.77}

The error originates from the uncertainties of the Mössbauer energies, given in [39,40].

In a similar way Bragg temperatures for ^{57}Fe and ^{161}Dy Mössbauer radiations which are close to each other, combined with the known temperature expansion in the direction $[1\,3\,\bar{4}\,28]$ – eq. (3.6) – allow us to determine the lattice constants in HEMEX sapphire at another temperature:

$$a = 4.7609(4)\ \text{Å}, \quad c = 12.99838(17)\ \text{Å} \quad \text{at} \quad T = 375.11\ \text{K}.$$

The experiments with ^{57}Fe, ^{151}Eu, ^{119}Sn, and ^{161}Dy Mössbauer radiations demonstrated that by using almost exact backscattering at different reflections in the same Al_2O_3 crystal one is able to obtain highly monochromatic radiation in a wide energy range of the X-ray spectrum.

5. Backscattering in combination with a moving resonant scatterer

A backscattering mirror reflects the beam back to the same sample, see figure 12. A resonator with two mirrors lets the beam pass though the sample many times (see, e.g., section 6). Multiple interaction of the beam with the sample then occurs and depends on the coherent properties of the beam: on its longitudinal (time) and lateral coherency.

Here we present the results of an experiment with a single backscattering mirror, which reflects synchrotron radiation pulses (14.413 keV) to a sample containing ^{57}Fe nuclei. The sample is a $\simeq$1.3 μm thick stainless steel (SS) foil of composition $Fe_{55}Cr_{25}Ni_{20}$ with iron enriched in ^{57}Fe to 95%. ^{57}Fe nuclei in SS exhibit an unsplit nuclear resonance. The nuclei behave as an ensemble of spatially coherent equivalent resonators which responds after excitation with enhanced re-emission of the resonant radiation in the forward direction.

The SS foil is placed 1 m in front of the mirror, thus the nuclear system is excited twice with a time lag of 6 ns by radiation pulses propagating in two opposite directions. The detector records time responses (spectra) on both excitations. In figure 12(a) the time spectrum is shown measured with the SS foil at rest. In figure 12(b) the time

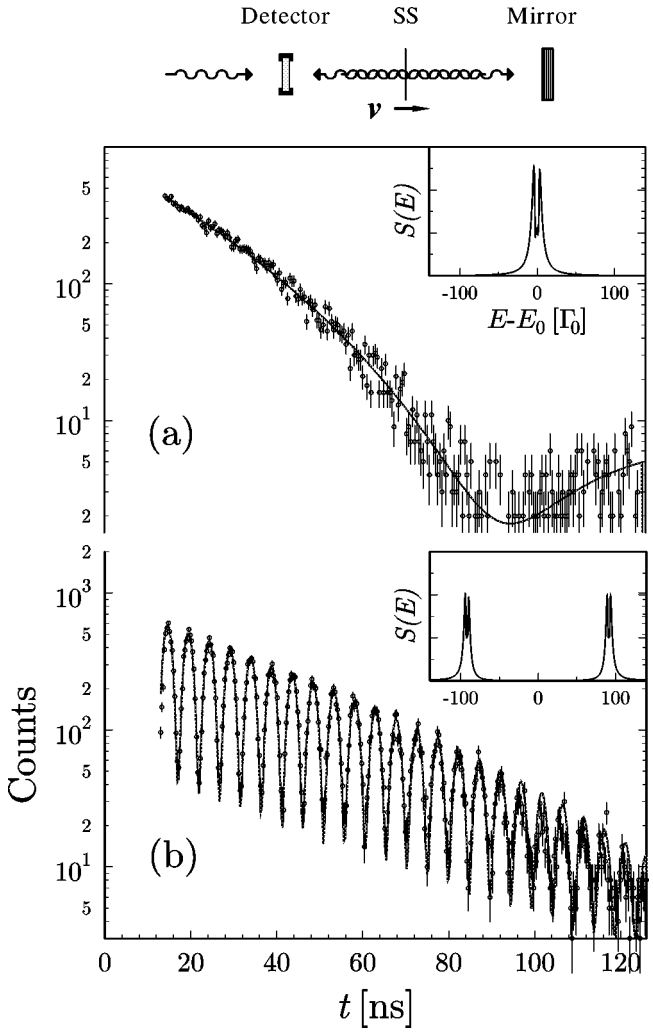

Figure 12. Time spectra of nuclear forward scattering (NFS) of synchrotron radiation measured with a backscattering mirror: (a) a single-resonance nuclear target SS ($\simeq$1.3 μm thick stainless steel foil) at rest: $v = 0$; (b) SS, moving with constant velocity v corresponding to a Doppler shift of $91.7\,\Gamma_0$, $\Gamma_0 = 4.8$ neV. (The measurements were performed at HASYLAB at the beamline BW4 by the authors in collaboration with J. Jäschke, M. Lucht, O. Leupold, U. van Bürck, W. Potzel and P. Schindelmann.) The solid lines are fits using the NFS theory [41,42]. The insets show the corresponding calculated energy spectra of NFS.

spectrum is shown measured with the SS foil moving with constant velocity v in the direction of the incident beam, producing a Doppler shift of the nuclear resonance in SS of $\Delta E_{\rm D} = (v/c)E = 91.7\,\Gamma_0$. $\Gamma_0 = 4.8$ neV is the natural linewidth. After reflection the beam sees the direction of v reversed with respect to the beam propagation direction. Thus, the nuclear resonance is shifted to $-91.7\,\Gamma_0$. The time spectra are fitted by using the model of nuclear resonant forward scattering in two samples which

are placed in a row. Without motion the nuclear resonance energies in both samples coincide. Thus, one expects scattering from a single resonance with a target of twice the effective thickness – see figure 12(a). An inspection of the measured curve supports this assumption. The minimum at about 93 ns is the minimum of a dynamical beat which is not seen in figure 12(b). If for some reason the energy of the reflected beam would be shifted and thus the incident and backscattered wave would have slightly different energies, the dynamical beat minimum would be shifted to earlier times [43,44]. The fit of the curve (a) yields no shift within the limits of a natural line width Γ_0.

The experiment can be interpreted as an ether drift experiment of the Michelson type. If the whole set-up is not at rest but moves with velocity u with respect to some universal frame the nuclear resonance is shifted to $E_0(1+u/c)$ and the forward scattering of delayed quanta takes place at this energy. After reflection by the moving mirror the energy of the quanta is changed to

$$E_0\left(1+\frac{u}{c}\right)-2\frac{u}{c}E_0\left(1+\frac{u}{c}\right)=E_0\left(1-\frac{u}{c}\right)-2\left(\frac{u}{c}\right)^2E_0.$$

$E_0(1-u/c)$ is the energy at which the resonance is seen by a γ-ray moving backwards. Thus, there remains a mismatch by the term $-2(u/c)^2E_0$. It is quadratic in u/c as in all experiments with closed path [45]. According to the analysis of the measurement (a) we get

$$2\left(\frac{u}{c}\right)^2E_0\leqslant\Gamma_0\quad\text{or}\quad\left(\frac{u}{c}\right)^2\leqslant\frac{1}{2}\frac{\Gamma_0}{E_0}\approx 1.8\cdot 10^{-13}$$

and

$$u\leqslant 4.2\cdot 10^{-7}c\simeq 126\ \text{ms}^{-1}$$

gives the lower level estimate of the velocity u. No systematic search for a possible ether drift was planned in this experiment. Thus, this result means that at the time of the experiment the laboratory component of the velocity with respect to a universal frame was below the given limit.

Finally, when the sample is moved the position of the resonance in "both" targets is shifted. This is proved by the observation of strong beating of two resonances spaced by $2\Delta E_{\mathrm{D}}=183.4\,\Gamma_0$, see figure 12(b).

The experiment and the simulations demonstrate that the backscattering mirror allows the radiation to interact coherently twice with the sample. Results of measurements with two samples are presented and discussed in [43].

6. Fabry–Pérot–Bragg étalon

As shown in the previous sections, sapphire crystals can be used as backscattering mirrors for hard X-rays. This makes backscattering resonators and interferometers in

this spectral region of electromagnetic radiation feasible. In the present section we analyse theoretically the properties of a Fabry–Pérot interferometer with single crystal sapphire mirrors for monochromatic 14.143 keV X-rays.

The Fabry–Pérot interferometer is commonly used in optics as a narrow-bandpass filter or as an instrument to measure spectral linewidths. It basically consists of two parallel mirrors separated by a gap ℓ_{gap}. Fabry–Pérot interferometers that cannot be scanned are called étalons. The normal modes of radiation, numbered here by n, which can be excited in the gap have energies $E_n = h\nu_n = (hc/2\ell_{\text{gap}})n$. The separation between the normal mode energies is

$$\Delta E_{\text{FP}} = E_{n+1} - E_n = \frac{hc}{2\ell_{\text{gap}}} \tag{6.1}$$

and, e.g., for a 1 mm gap $\Delta E_{\text{FP}} = 0.62$ meV ($\Delta\nu_{\text{FP}} = 1.5 \cdot 10^{11}$ Hz). The spectral width of these modes depend on the reflectivity and transmissivity of the mirrors. The relative width can be made very small provided the reflectivity of the mirrors is high. The theory of the optical Fabry–Pérot interferometer is well developed [46].

A first design of a Fabry–Pérot-type interferometer for X-rays was proposed by Steyerl and Steinhauser [47]. The theory of the Fabry–Pérot–Bragg étalon based on the dynamical theory of X-ray diffraction in perfect crystals was given in references [48,49]. The latter unfortunately contains misprints. We will give here independently a short derivation of the expressions for reflectivity and transmissivity of the Fabry–Pérot–Bragg étalon. A more general theory of the Fabry–Pérot–Bragg interferometer, which takes into account a possible translation of the reflecting planes of both mirrors, surface roughness, and possible misalignment (rotation) of the crystals is considered in [50].

It will be assumed that the mirrors of our device are parts of a common crystal. No translation of the reflecting planes is possible. We shall refer to such an instrument as a Fabry–Pérot–Bragg étalon.

The amplitude r_{FP} of the radiation reflected from the Fabry–Pérot–Bragg étalon and the amplitude t_{FP} of the radiation transmitted through the Fabry–Pérot–Bragg étalon can be derived by summing the amplitudes of all possible multiple scattering paths. With each path a probability amplitude is associated for an incident beam to arrive at the final point, which is a product of successive reflection and transmission amplitudes in both crystal plates of the Fabry–Pérot–Bragg étalon and its gap.[8] By using the notations of figure 13 we obtain:

$$r_{\text{FP}} = r_{0H} + t_{00}\mathrm{e}^{\mathrm{i}\phi}\tilde{r}_{0H}\mathrm{e}^{\mathrm{i}\tilde{\phi}}\big(t_{HH} + r_{H0}\mathrm{e}^{\mathrm{i}\phi}\tilde{r}_{0H}\mathrm{e}^{\mathrm{i}\tilde{\phi}}(t_{HH} + \cdots,$$
$$t_{\text{FP}} = t_{00}\mathrm{e}^{\mathrm{i}\phi}\big(\tilde{t}_{00} + \tilde{r}_{0H}\mathrm{e}^{\mathrm{i}\tilde{\phi}}r_{H0}\mathrm{e}^{\mathrm{i}\phi}\big(\tilde{t}_{00} + \cdots.$$

[8] This way of derivation, although illustrative, is based mostly on intuition. A self-consistent derivation of the reflectivity and transmissivity of the Fabry–Pérot–Bragg étalon is given in [50].

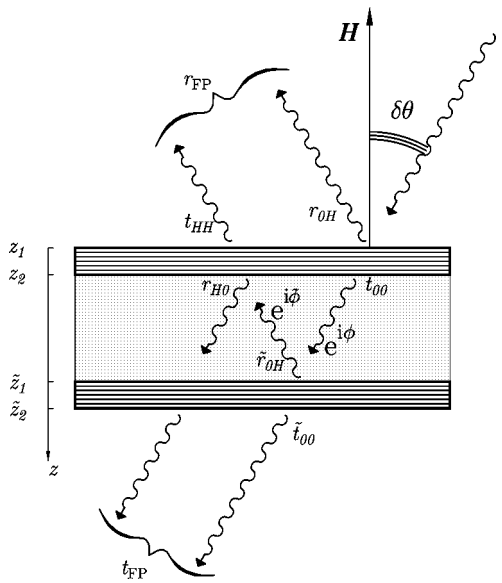

Figure 13. The Fabry–Pérot–Bragg étalon with two parallel single crystal plates used as reflecting mirrors. The crystals have a thickness $\ell = z_2 - z_1$ and $\tilde{\ell} = \tilde{z}_2 - \tilde{z}_1$ separated by a gap $\ell_{\text{gap}} = \tilde{z}_1 - z_2$ filled with nondiffracting medium. Scheme of the multiple scattering and the amplitudes of the individual scattering events r_{0H}, r_{H0}, etc. are shown.

The summation of the series of multiple scattering amplitudes results in

$$r_{\text{FP}} = r_{0H} + \frac{t_{00}t_{HH}\tilde{r}_{0H}\mathrm{e}^{\mathrm{i}(\phi+\tilde{\phi})}}{1 - r_{H0}\tilde{r}_{0H}\mathrm{e}^{\mathrm{i}(\phi+\tilde{\phi})}}, \qquad t_{\text{FP}} = \frac{t_{00}\tilde{t}_{00}\mathrm{e}^{\mathrm{i}\phi}}{1 - r_{H0}\tilde{r}_{0H}\mathrm{e}^{\mathrm{i}(\phi+\tilde{\phi})}}. \tag{6.2}$$

$\exp(\mathrm{i}\phi)$ and $\exp(\mathrm{i}\tilde{\phi})$ are the transmission amplitudes through the gap for the radiation propagating in the direction of the incident and of the reflected beam, respectively. The complex phases ϕ and $\tilde{\phi}$ are due to refraction in the gap:

$$\phi = \frac{K\ell_{\text{gap}}}{2\gamma_0}\chi_0^{\text{gap}}, \qquad \tilde{\phi} = \frac{K\ell_{\text{gap}}}{2\gamma_0}\left(\chi_0^{\text{gap}} - \alpha\right). \tag{6.3}$$

Here χ_0^{gap} is the Fourier component of zero order of the electric susceptibility of the medium filling the gap, cf. eqs. (A.1) and (A.2) of the appendix. The phase $\tilde{\phi}$ contains, additionally to ϕ, a shift which results from the difference of the values of the wave vectors of the incident K_0 and reflected K_H waves: $K_H - K_0 = \alpha K/2$, which is obtained from eq. (A.9) of the appendix, α is the deviation from Bragg's condition defined in appendix A.2.

The amplitude of the radiation r_{0H} reflected from the top side of the first crystal is given by the expression

$$r_{0H} = R_1 R_2 \frac{1 - \mathrm{e}^{\mathrm{i}(\delta_1 - \delta_2)\ell}}{R_2 - R_1\mathrm{e}^{\mathrm{i}(\delta_1 - \delta_2)\ell}}, \tag{6.4}$$

which is obtained from eq. (A.27) of the appendix by using the definitions $r_{0H} = E_H(z_1)$ and $\ell = z_2 - z_1$.

The transmission t_{00} through the first crystal of the radiation incident on the crystal is $E_0(z_2)$ of eq. (A.26) of the appendix and is given by

$$t_{00} = \mathrm{e}^{\mathrm{i}\delta_1\ell}\frac{R_2 - R_1}{R_2 - R_1\mathrm{e}^{\mathrm{i}(\delta_1-\delta_2)\ell}}. \tag{6.5}$$

To evaluate reflection and transmission of the radiation incident on the bottom of the crystals we use eqs. (A.28), (A.29) of the appendix. By using the definitions $r_{H0} = E_0(z_2)$ and $t_{HH} = E_H(z_1)$ we obtain

$$r_{H0} = \frac{1 - \mathrm{e}^{\mathrm{i}(\delta_1-\delta_2)\ell}}{R_2 - R_1\mathrm{e}^{\mathrm{i}(\delta_1-\delta_2)\ell}}, \tag{6.6}$$

$$t_{HH} = \mathrm{e}^{-\mathrm{i}\delta_2\ell}\frac{R_2 - R_1}{R_2 - R_1\mathrm{e}^{\mathrm{i}(\delta_1-\delta_2)\ell}}. \tag{6.7}$$

For the reflection and transmission amplitudes of the second crystal, $\tilde{r}_{0H}$, $\tilde{r}_{H0}$, $\tilde{t}_{00}$, $\tilde{t}_{HH}$, the same equations (6.4)–(6.7) are valid, however, with the substitution of ℓ by $\tilde{\ell}$.

The $\delta_{1,2}$ and $R_{1,2}$ entering expressions (6.4)–(6.7) for reflectivity and transmissivity of the Bragg mirrors are functions of the parameter α – the deviation from Bragg's condition – only, as discussed in appendix A.3. The parameter α is a function of the energy E and the angle of incidence θ of the X-ray, as well as of the crystal temperature T. The latter controls the Bragg energy of the reflection. Thus, reflectivity and transmissivity of the Fabry–Pérot–Bragg étalon, given by eq. (6.2), can also be expressed as functions of the parameter α: $r_{\mathrm{FP}}(\alpha)$, $t_{\mathrm{FP}}(\alpha)$. The energy, angular, and temperature dependences of reflectivity and transmissivity are obtained from $r_{\mathrm{FP}}(\alpha)$, $t_{\mathrm{FP}}(\alpha)$ by using the dependences of α on E, θ, and T, respectively, given by eq. (A.11) or (A.18) of the appendix.

The results of numerical calculations of the energy and angular dependence of transmissivity and reflectivity of the Fabry–Pérot–Bragg étalon performed with eqs. (6.2)–(6.7) of the present section are shown in figures 14 and 15. Calculations for four different values of the gap ℓ_{gap} between the sapphire $(1\,3\,\bar{4}\,28)$ Bragg mirrors are shown. The dependences labelled with (a) correspond to a zero gap ($\ell_{\mathrm{gap}} = 0$), i.e., to a single crystal plate of thickness $\ell + \tilde{\ell}$. The dependences show the region of high reflectivity and respectively very low transmissivity typical for Bragg diffraction as discussed, e.g., in appendix A.3. The superimposed oscillation is a result of the finite crystal thickness $\ell + \tilde{\ell}$.

The transmissivity with nonzero gaps marked by (b), (c), or (d) in figure 14 shows sharp maxima with spacing ΔE_{FP} given by eq. (6.1) in the region of initially low transmissivity. Normal incidence of the plane monochromatic wave to the reflecting planes $(1\,3\,\bar{4}\,28)$ is assumed. The reflectivity shows sharp minima at the same positions. The calculations demonstrate that the Fabry–Pérot–Bragg étalon behaves similar to the optical Fabry–Pérot étalon in the region of high reflectivity. At well-defined X-ray

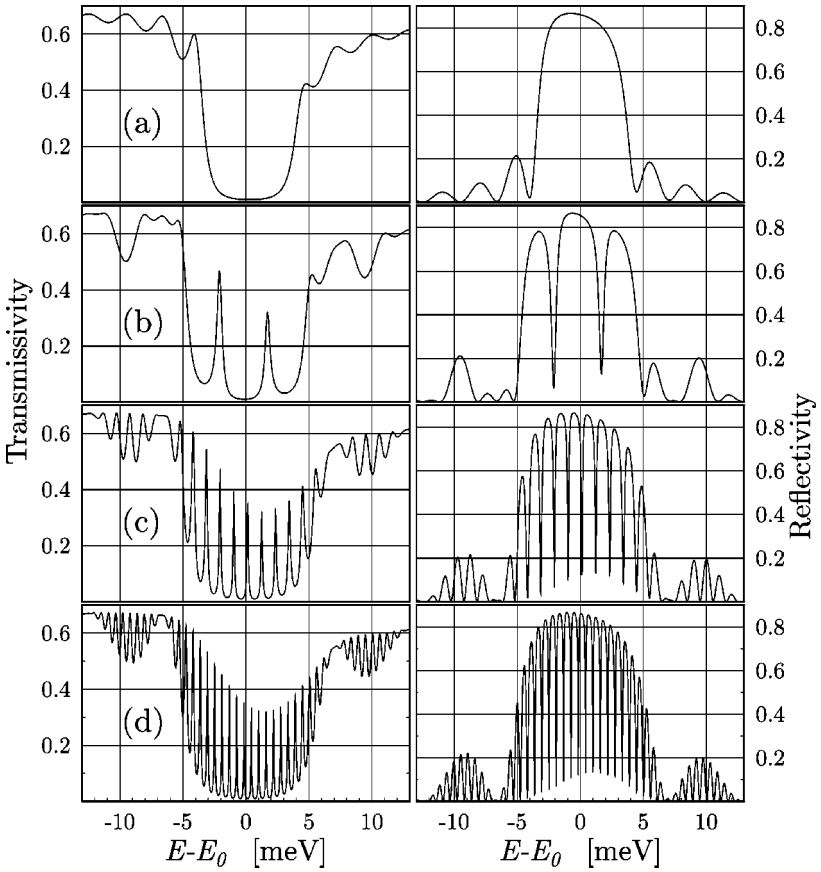

Figure 14. Energy spectrum of X-rays ($E_0 = 14.413$ keV) transmitted through (left) or reflected from (right) the Fabry–Pérot–Bragg étalon made of two single crystal plates of Al_2O_3 with Bragg-reflecting planes $(1\,3\,\bar{4}\,28)$ parallel to the surfaces (figure 13). The crystal temperature is $T = 373.11$ K. The radiation is a plane monochromatic wave at normal incidence to the reflecting planes ($\delta\theta = 0$). The thicknesses of the Bragg mirrors are $\ell = \tilde{\ell} = 100$ μm. The gap between the mirrors in vacuum is taken to be (a) $\ell_{\rm gap} = 0$, (b) $\ell_{\rm gap} = 200$ μm, (c) $\ell_{\rm gap} = 500$ μm, (d) $\ell_{\rm gap} = 1000$ μm.

energies (angles of incidence) a system of two strongly reflecting parallel Bragg mirrors becomes transparent.

To ensure an observation of the sharp transmission peaks in the energy spectra of figure 14 one has to use an X-ray beam with a sufficiently high angular collimation. As one can see from the angular dependences shown in figure 15, the larger the gap between the mirrors, the less divergent the incident beam should be. For $\ell_{\rm gap} = 1$ mm, e.g., the divergence of the incident beam should be $\leqslant 20$ μrad. Along with the very good collimation the incident X-rays have to have a monochromatization better than $\Delta E_{\rm FP}$, i.e., it should be in the sub-meV region for 14.4 keV X-rays and even sharper for X-rays with higher energy.

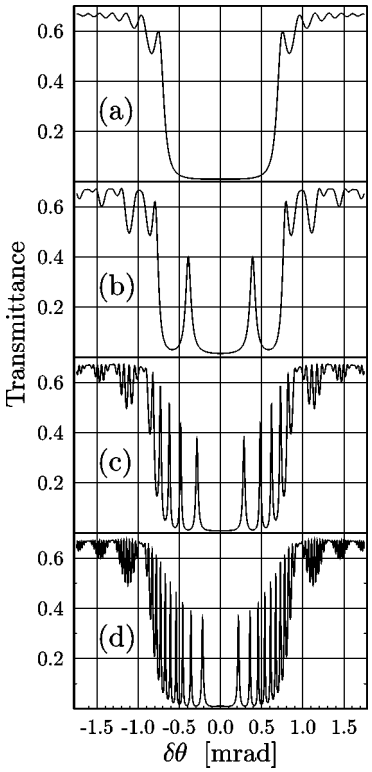

Figure 15. Angular dependence of transmissivity of X-rays ($E_0 = 14.413$ keV) through a Fabry–Pérot–Bragg étalon (figure 13) made of two single crystal plates of Al_2O_3 with Bragg-reflecting planes $(1\,3\,\bar{4}\,28)$ parallel to the surfaces. $\delta\theta$ is the angular deviation from normal incidence of the X-rays to the $(1\,3\,\bar{4}\,28)$ reflecting planes. The crystal temperature is $T = 373.11$ K. The radiation is a plane monochromatic wave at normal incidence to the reflecting planes. The thicknesses of the Bragg mirrors are $\ell = \tilde{\ell} = 100$ μm. The gap between the mirrors in vacuum is taken to be (a) $\ell_{\rm gap} = 0$, (b) $\ell_{\rm gap} = 200$ μm, (c) $\ell_{\rm gap} = 500$ μm, (d) $\ell_{\rm gap} = 1000$ μm.

7. Conclusions

We have presented results of comprehensive experimental studies of exact backscattering in the two-beam diffraction case in sapphire (Al_2O_3) single crystals. The peak reflectivity, the angular and energy dependences were measured by using highly monochromatic and well collimated X-rays. The dynamical theory of diffraction in perfect crystals qualitatively agrees with our results. We also point out discrepancies: the wings of energy profiles are better described by a Lorentzian rather than by a Darwin–Prins profile. We attribute this to a not sufficient perfection of the sapphire crystals used.

We have also measured energy profiles of reflectivity at normal incidence to atomic planes (12 4 0) of a silicon single crystal. In this case multiple beam scattering effects (24 beams are involved rather than 2 in the case of Al_2O_3) play a significant

role. The reflectivity drops by more than a factor of 2 and the energy dependence of exact backscattering has three apparent peaks with different widths.

Crystals with noncubic symmetry, like Al_2O_3, BeO, Be, noncubic polytypes of SiC, suit better than, e.g., cubic Si crystals, for use as backscattering mirrors. First, due to the fact that Bragg energies (X-ray energies for which peak reflectivity in exact backscattering takes place) are much less degenerate and thus backscattering is realised for X-rays of practically any energy. Fine tuning of the crystal lattice and thus of Bragg energies is performed by changing the crystal temperature. Second, exact backscattering in Si crystals is practically impossible, because of the multiple beam scattering effects.

Exact backscattering in Al_2O_3 was observed for 14.4125 keV Mössbauer radiation of ^{57}Fe [2], 21.5415 keV Mössbauer radiation of ^{151}Eu [37], 23.8795 keV radiation of ^{119}Sn [37], and 25.6513 keV radiation of ^{161}Dy [38]. Experiments with ^{57}Fe, ^{151}Eu, ^{119}Sn, and ^{161}Dy Mössbauer radiations demonstrate that by using backscattering in one and the same Al_2O_3 crystal one is able to obtain highly monochromatic radiation in a wide energy range of the X-ray spectrum.

The performance of the sapphire Bragg mirror as part of a backscattering resonator was demonstrated.

A concrete design of a Fabry–Pérot–Bragg étalon and simulations of energy and angular dependences of transmissivity and reflectivity for 14.413 keV X-rays are presented and sapphire crystals with a $(1\,3\,\bar{4}\,28)$ Bragg reflection have been used as backscattering mirrors.

Acknowledgements

The work was supported by the Bundesministerium für Bildung, Forschung und Technologie under Contract No. 05 643GUA1. The authors are indebted to H. de Waard, E. Alp, and H.-C. Wille for reading the manuscript.

Appendix A. Dynamical theory of backscattering

We will recall here elements of the dynamical theory of diffraction of X-rays in perfect crystals laying emphasis on the points critical in the backscattering geometry. The equations will be derived that are used in the present paper for evaluation of angular, energy, and temperature dependences of the crystal reflectivity in backscattering as well as for the evaluation of the reflectivity and transmissivity of Fabry–Pérot–Bragg étalons.

The dynamical theory of diffraction in backscattering geometry is discussed in [4–7]. Our derivation is similar to that of Caticha and Caticha-Ellis [6]. It is based on the perception that the basic equations of dynamical diffraction theory as they were derived by von Laue [51] (see also [52–54]) are valid in backscattering geometry as well. However, the parameter α of deviation from the Bragg condition should be defined

slightly differently. In [6] a new expression for α, valid in backscattering geometry, was derived. A more general expression for α, valid for any angle of incidence, was given in [2] and is derived here.

A.1. General equations

The scattering geometry is shown in figure 16. The wave vectors $\boldsymbol{K}_0$ and $\boldsymbol{K}_H$ of the incident and scattered radiation in vacuum define the scattering plane $(\boldsymbol{K}_0, \boldsymbol{K}_H)$. Diffraction takes place on the atomic planes of a crystal, which are perpendicular to the reciprocal vector $\boldsymbol{H}$. The unit vector $\hat{\boldsymbol{z}}$ is a normal to the crystal surface directed inwards.

The equations of the dynamical theory will be derived by using an approach first formulated by von Laue [51] (see also [52–54]). It is based on the solution of Maxwell's equations for a medium with an electric susceptibility that continuously varies and is periodic in space:

$$\chi(\boldsymbol{r}) = \sum_H \chi_H \mathrm{e}^{\mathrm{i}\boldsymbol{H}\boldsymbol{r}}. \tag{A.1}$$

The Fourier components of the susceptibility $\chi_0, \chi_H, \chi_{\bar{H}}$, etc. are determined by

$$\chi_H = -r_\mathrm{e}\frac{\lambda^2}{\pi V}F_H \tag{A.2}$$

with

$$F_H = \sum_\mathrm{n} f_\mathrm{n}(\boldsymbol{H})\mathrm{e}^{\mathrm{i}\boldsymbol{H}\boldsymbol{r}_\mathrm{n}}\mathrm{e}^{-W_\mathrm{n}(\boldsymbol{H})} \tag{A.3}$$

the structure factor of the crystal unit cell, f_n the atomic scattering amplitude (with anomalous scattering corrections) and $\exp(-2W_\mathrm{n})$ the Debye–Waller factor of an atom located in the unit cell at a point with radius vector $\boldsymbol{r}_\mathrm{n}$; V is the unit cell volume and r_e is the classical electron radius.

The incident monochromatic plane wave $\boldsymbol{\epsilon}^s\exp[\mathrm{i}(\boldsymbol{K}_0\boldsymbol{r} - Et/\hbar)]$ ($|\boldsymbol{K}_0| = K = E/\hbar c = 2\pi/\lambda$) in the polarization state $\boldsymbol{\epsilon}^s$ ($s = \{\sigma, \pi\}, |\boldsymbol{\epsilon}^s| = 1$) excites a radiation

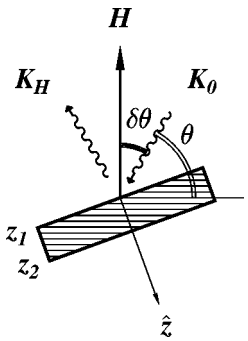

Figure 16. Scattering geometry.

field $E^s(\boldsymbol{r},t)$ inside the crystal in the form of a Bloch wave, which in the two-beam approximation is given by

$$E^s(\boldsymbol{r},t)=\mathrm{e}^{-\mathrm{i}Et/\hbar}\left[E_0^s\mathrm{e}^{\mathrm{i}\boldsymbol{k}_0\boldsymbol{r}}+E_H^s\mathrm{e}^{\mathrm{i}\boldsymbol{k}_H\boldsymbol{r}}\right], \tag{A.4}$$

where $\boldsymbol{k}_0$ and $\boldsymbol{k}_H$ are in-crystal wave vectors of the incident and diffracted radiation, respectively, which are related by conservation of momentum in crystals:

$$\boldsymbol{k}_H=\boldsymbol{k}_0+\boldsymbol{H}. \tag{A.5}$$

Because of the refraction, although small, the in-crystal wave vectors $\boldsymbol{k}_{0,H}$ differ from those in vacuum $\boldsymbol{K}_{0,H}$:

$$\boldsymbol{k}_{0,H}=\boldsymbol{K}_{0,H}+\delta\hat{\boldsymbol{z}}. \tag{A.6}$$

This relation is derived from the condition of continuity of the tangential component of the radiation at the vacuum–crystal interface. Along with δ we shall use the parameter $\varepsilon=\delta\gamma_0/K$ ($\gamma_0=\hat{\boldsymbol{z}}\boldsymbol{K}_0/K$).

Substitution of the radiation field in the crystal in the form given by eqs. (A.4), (A.5), and (A.6) into Maxwell's equations with the electric susceptibility eq. (A.1) results in the following set of algebraic equations for the amplitudes of the transmitted E_0^s and diffracted E_H^s radiation components:

$$\begin{aligned}(2\varepsilon-\chi_0)\,E_0^s-\chi_{\bar{H}}C^sE_H^s&=0,\\ -\chi_HC^s\,E_0^s+(2\varepsilon/b-\chi_0+\alpha)E_H^s&=0.\end{aligned} \tag{A.7}$$

Let us first discuss the parameters $\alpha,\ b,\ C^s$ of this set of equations.

The asymmetry parameter

$$b=\frac{\hat{\boldsymbol{z}}\boldsymbol{K}_0}{\hat{\boldsymbol{z}}\boldsymbol{K}_H} \tag{A.8}$$

characterizes how symmetrically the wave vectors of the incident and reflected radiation are directed with respect to the normal of the crystal surface. In the reflection scattering geometry, the so-called Bragg geometry, as in figure 16, the asymmetry parameter takes arbitrary negative values. If the wave vectors of the incident and reflected beams make the same angle with the normal to the crystal surface, then $b=-1$. This is always the case for exact backscattering.

The polarization factor $C^\sigma=1$ and $C^\pi=\cos 2\theta$. As long as our primary interest here is backscattering, for which $|C^s|^2\simeq 1$ for both polarizations, we will not distinguish in the following between the solutions of eq. (A.7) for different polarization components and will omit for simplicity the polarization index s.

A.2. Deviation from Bragg's condition

The parameter

$$\alpha=\frac{\boldsymbol{K}_H^2-\boldsymbol{K}_0^2}{K^2} \tag{A.9}$$

is a measure of the deviation from Bragg's condition (2.1). Indeed, if $\alpha = 0$ then $K_0 = K_H$ and with eq. (A.5) one obtains the kinematical Bragg law in the form $H = 2K\sin\theta$, equivalent to eq. (2.1).

The dimensionless parameter α plays an important role in our considerations since the reflectivity (transmissivity) can be presented as a function of only this parameter, as shown in the next section. The sought for angular, energy, and temperature dependences of the reflectivity and transmissivity are then defined by using an $\alpha = f(E,\theta,T)$ dependence. It is this dependence $\alpha = f(E,\theta,T)$ which should be carefully specified for the dynamical theory to be applicable for backscattering. This dependence is derived here.

We make use of definition (A.9). With figure 16 and the relation $\boldsymbol{K}_H = \boldsymbol{K}_0 + \boldsymbol{H}$ the parameter α is

$$\alpha = \frac{1}{K^2}\left(-2KH\sin\theta + H^2\right). \tag{A.10}$$

Bearing in mind that $H = 2\pi/d_{hkl} = 2E_{hkl}/\hbar c$ and $K = \omega/c = E/\hbar c$, α may be presented as a function of the angle of incidence θ, the energy E, and the Bragg energy $E_{hkl}(T)$ in the following way [2]:

$$\alpha = 4\frac{E_{hkl}(T)}{E}\left[\frac{E_{hkl}(T)}{E} - \sin\theta\right]. \tag{A.11}$$

This expression is valid for any angle of incidence θ, including $\theta = \pi/2$. It is the sought for general dependence $\alpha = f(E,\theta,T)$ for the given value of the Bragg energy E_{hkl}.

By using the X-ray wavelength λ instead of energy E and d_{hkl} instead of E_{hkl} we obtain the equivalent dependence

$$\alpha = \frac{2\lambda}{d_{hkl}(T)}\left[\frac{\lambda}{2d_{hkl}(T)} - \sin\theta\right]. \tag{A.12}$$

By using the kinematical Bragg law, eq. (2.1), α can be expressed via the kinematical Bragg angle θ_{B}:

$$\alpha = 4\sin\theta_{\mathrm{B}}[\sin\theta_{\mathrm{B}} - \sin\theta]. \tag{A.13}$$

Assuming that $|\theta_{\mathrm{B}} - \theta| \ll 1$ one easily derives from eq. (A.13) the standard approximation for α normally used in the dynamical theory [53,54]:

$$\alpha = 2(\theta_{\mathrm{B}} - \theta)\sin 2\theta_{\mathrm{B}}. \tag{A.14}$$

However, this expression fails to work in the region of backscattering: $\theta_{\mathrm{B}} = \pi/2$.

As was shown in [6] another approximation of α is applicable for backscattering:

$$\alpha = 2\left[\delta\theta^2 - \frac{2(E - E_{hkl})}{E_{hkl}}\right]. \tag{A.15}$$

This expression is easily derived from the general expression (A.11) for α, assuming $|\delta\theta| \ll 1$ and $|(E - E_{hkl})/E_{hkl}| \ll 1$.

Due to the fact that the interplanar distance d_{hkl} and, therefore, the Bragg energy is temperature-dependent, α can be changed by varying the temperature. Taking into account that the variation of the Bragg energy in a small temperature range can be expressed as

$$E_{hkl}(T+\delta T) = E_{hkl}(T)(1-\beta_{hkl}\delta T), \tag{A.16}$$

with

$$\beta_{hkl} = \frac{1}{d_{hkl}(T)}\frac{\mathrm{d}d_{hkl}}{\mathrm{d}T} \tag{A.17}$$

the linear temperature expansion coefficient in the direction $[hkl]$, we obtain for α the following expression:

$$\alpha = 2\delta\theta^2 - 4\left[\frac{\delta E}{E_{hkl}(T)} + \beta_{hkl}(T)\delta T\right]. \tag{A.18}$$

Here $\delta E = E - E_{hkl}(T)$. The equation shows that α varies linearly both with X-ray energy and crystal temperature, and quadratically with the angular deviation $\delta\theta$.

Equation (A.18) can be used to establish the relation of equivalence between the variations of X-ray energy and crystal temperature. Those values of E and T are equivalent which result in the same reflectivity. As long as the reflectivity of X-rays is a function of α only, we obtain from eq. (A.18) the E–T equivalence relation:

$$\delta E = E_{hkl}(T)\beta_{hkl}(T)\delta T. \tag{A.19}$$

A.3. Reflectivity and transmissivity

The compatibility conditions for the set of linear equations (A.7) determine two possible values of ε:

$$2\varepsilon_{(1,2)} - \chi_0 = C\sqrt{|b|\chi_H\chi_{\bar{H}}}\left[-y \pm \sqrt{y^2 + \frac{b}{|b|}}\right]. \tag{A.20}$$

Here

$$y = \frac{\chi_0(1-b) + \alpha b}{2C\sqrt{|b|\chi_H\chi_{\bar{H}}}}. \tag{A.21}$$

It is assumed that the imaginary part of the root in eq. (A.20) is positive and index 1 in ε_1 corresponds to the sign "+", i.e., $\mathrm{Im}(\varepsilon_1 - \varepsilon_2) > 0$. With account of the two possible solutions (A.20) for ε, expression eq. (A.4) for the radiation field in the crystal reads

$$E(\boldsymbol{r}, t) = \mathrm{e}^{\mathrm{i}\boldsymbol{K}_0\boldsymbol{r} - \mathrm{i}Et/\hbar}\left[E_0(z) + E_H(z)\,\mathrm{e}^{\mathrm{i}\boldsymbol{H}\boldsymbol{r}}\right], \tag{A.22}$$

with

$$E_0(z) = \sum_{\nu=1,2} \mathrm{e}^{\mathrm{i}\delta_\nu z}E_0^{(\nu)}, \qquad E_H(z) = \sum_{\nu=1,2} \mathrm{e}^{\mathrm{i}\delta_\nu z}E_H^{(\nu)}, \quad \delta_\nu = \frac{K}{\gamma_0}\varepsilon_\nu. \tag{A.23}$$

By using eq. (A.7) one can define the ratio of the amplitudes $E_0^{(1,2)}$ and $E_H^{(1,2)}$:

$$R_{(1,2)} = \frac{E_H^{(1,2)}}{E_0^{(1,2)}} = \frac{2\varepsilon_{(1,2)} - \chi_0}{C\chi_{\bar{H}}}. \tag{A.24}$$

To define the amplitudes $E_0^{(1,2)}$ and $E_H^{(1,2)}$ themselves additional information is needed. It can be obtained from the boundary condition $E_0(z_1) = 1$ at the entrance surface $z = z_1$ for the beam propagating in the forward direction and from the boundary condition $E_H(z_2) = 0$ at the exit surface $z = z_2$ for the reflected beam, see figure 16. By using eqs. (A.23), they can be written as

$$\begin{aligned} E_0^{(1)} \exp[\mathrm{i}\delta_1 z_1] + E_0^{(2)} \exp[\mathrm{i}\delta_2 z_1] = 1, \\ E_H^{(1)} \exp[\mathrm{i}\delta_1 z_2] + E_H^{(2)} \exp[\mathrm{i}\delta_2 z_2] = 0. \end{aligned} \tag{A.25}$$

As a result the forward $E_0(z)$ and Bragg scattered $E_H(z)$ components of the radiation field eq. (A.22) inside the crystal at a depth z are given by

$$E_0(z) = \frac{R_1 \exp[\mathrm{i}\delta_2(z - z_2)] - R_2 \exp[\mathrm{i}\delta_1(z - z_2)]}{R_1 \exp[\mathrm{i}\delta_2(z_1 - z_2)] - R_2 \exp[\mathrm{i}\delta_1(z_1 - z_2)]}, \tag{A.26}$$

$$E_H(z) = \frac{R_1 R_2 \{\exp[\mathrm{i}\delta_2(z - z_2)] - \exp[\mathrm{i}\delta_1(z - z_2)]\}}{R_1 \exp[\mathrm{i}\delta_2(z_1 - z_2)] - R_2 \exp[\mathrm{i}\delta_1(z_1 - z_2)]}. \tag{A.27}$$

For the problem of the Fabry–Pérot–Bragg étalon addressed in section 6 it is helpful also to consider the case of the entrance surface at z_2 and the incident radiation with the wave vector $\boldsymbol{K}_H$ rather than with $\boldsymbol{K}_0$. In this case the boundary conditions are written as

$$\begin{aligned} E_0^{(1)} \exp[\mathrm{i}\delta_1 z_1] + E_0^{(2)} \exp[\mathrm{i}\delta_2 z_1] = 0, \\ E_H^{(1)} \exp[\mathrm{i}\delta_1 z_2] + E_H^{(2)} \exp[\mathrm{i}\delta_2 z_2] = 1, \end{aligned} \tag{A.28}$$

resulting in the solution:

$$E_0(z) = \frac{\exp[\mathrm{i}\delta_2(z - z_1)] - \exp[\mathrm{i}\delta_1(z - z_1)]}{R_2 \exp[\mathrm{i}\delta_2(z_2 - z_1)] - R_1 \exp[\mathrm{i}\delta_1(z_2 - z_1)]}, \tag{A.29}$$

$$E_H(z) = \frac{R_2 \exp[\mathrm{i}\delta_2(z - z_1)] - R_1 \exp[\mathrm{i}\delta_1(z - z_1)]}{R_2 \exp[\mathrm{i}\delta_2(z_2 - z_1)] - R_1 \exp[\mathrm{i}\delta_1(z_2 - z_1)]}. \tag{A.30}$$

The reflectivity of the crystal is the ratio of the fluxes in the incident and in the reflected beams:

$$R = \frac{1}{|b|} \frac{|E_H(z_{\mathrm{in}})|^2}{|E_0(z_{\mathrm{in}})|^2}, \tag{A.31}$$

where for incidence from the front side $z_{\mathrm{in}} = z_1$ and eqs. (A.26)–(A.27) should be used, while for incidence from the opposite side $z_{\mathrm{in}} = z_2$ and eqs. (A.29)–(A.30) should be used. In the approximation of a semi-infinite crystal for which $\mathrm{Im}(\delta_1 - \delta_2)(z_2 - z_1) \gg 1$ the expression for the reflectivity (A.31) using eqs. (A.26)–(A.27) – front side incidence

– reduces to $R = R_1/|b|$. By using eqs. (A.20), (A.24) we obtain the well-known expression for the reflectivity in the approximation of a semi-infinite crystal:

$$R = \left|\frac{\chi_H}{\chi_{\bar{H}}}\right| \left| -y \pm \sqrt{y^2 + \frac{b}{|b|}} \right|^2. \tag{A.32}$$

The reflectivity is a function of the parameter y alone.

Let us first assume that y is real. This happens in the absence of photo-absorption, or when the photo-absorption can be neglected: $\mathrm{Im}\{\chi_{0,H}\} \ll \mathrm{Re}\{\chi_{0,H}\}$. We assume also that $\chi_H = \chi_{\bar{H}}$, which is true for centrosymmetric crystals. Under these conditions the reflectivity equals unity in the region $y^2 \leqslant b/|b|$, usually referred to as the region of total reflection. Taking into account eq. (A.21) the region of total reflection can be defined by the parameter α as

$$\alpha_{-1} \leqslant \alpha \leqslant \alpha_{+1}, \tag{A.33}$$

$$\alpha_{\pm 1} = \alpha_0 \pm 2C\sqrt{\frac{\chi_H \chi_{\bar{H}}}{|b|}}, \quad \alpha_0 = \chi_0\left(1 - \frac{1}{b}\right). \tag{A.34}$$

The centre of the region of total reflection is shifted from the kinematical position $\alpha = 0$ by $\alpha_0 = \chi_0(1 - 1/b)$ due to refraction. For instance, X-rays at normal incidence ($\delta\theta = 0, b = -1$) are reflected at an energy

$$E = E_{hkl}\left(1 - \frac{\chi_0}{2}\right) \equiv \widetilde{E}_{hkl}, \tag{A.35}$$

which is shifted by $\delta E = -\chi_0 E_{hkl}/2$ from the kinematical Bragg energy E_{hkl}. The shift is positive, as $\chi_0 < 0$. $\widetilde{E}_{hkl}$ will be referred to as the dynamical Bragg energy. The width of the region of total reflection,

$$\Delta\alpha = \alpha_{+1} - \alpha_{-1} = 4C\sqrt{\chi_H \chi_{\bar{H}}/|b|}, \tag{A.36}$$

is of the order of $|\sqrt{\chi_H \chi_{\bar{H}}}| \leqslant 10^{-6}$. To define the width of the reflection region in units of the angle of incidence θ, X-ray energy E, or crystal temperature T an $\alpha = f(\theta, E, T)$ dependence should be used, e.g., expressed by eq. (A.18), which is valid in backscattering geometry.

According to eqs. (A.18), (A.33), (A.34) already tiny variations of E, θ or T produce sizable changes in reflectivity. These variations, however, leave the components of the electric susceptibility χ_0, χ_H, asymmetry parameter b, and polarization factor C entering along with α the variable y practically unchanged. From this we conclude that the reflectivity can be expressed as a function $R(\alpha)$. If $R(\alpha)$ is known, by using $\alpha = f(\theta, E, T)$ presented in appendix A.2, the reflectivity as a function of angle of incidence, photon energy and crystal temperature can be immediately derived.

Taking into account photo-absorption or a crystal of finite thickness requires the application of general eqs. (A.26)–(A.31) for calculations of the reflectivity. Maximum reflectivity and its position α_0, as well as the width in the reflection curve $\Delta\alpha =$

$\alpha_{+1} - \alpha_{-1}$, can be derived by numerical calculations. It will be different from $\delta\alpha$ given by eq. (A.36), but still of the order $|\chi_H| \leqslant 10^{-5}$. Also the conclusion, that the reflectivity is a function of α, only stays intact in the general case.

From numerical calculations one defines $R(\alpha)$, maximum reflectivity $R(\alpha_0)$, its position α_0 and its half width $\Delta\alpha$. All these dependences and values can be easily expressed in the units of the variables θ, E, or T by using a valid relation $\alpha = f(\theta, E, T)$ presented in appendix A.2.

References

[1] C. Cusatis, D. Udron, I. Mazzaro, C. Giles and H. Tolentino, Acta Cryst. A 52 (1996) 614.
[2] Yu.V. Shvyd'ko, E. Gerdau, J. Jäschke, O. Leupold, M. Lucht and H.D. Rüter, Phys. Rev. B 57 (1998) 4968.
[3] S. Kikuta, Y. Imai, T. Iizuka, Y. Yoda, X.-W. Zhang and K. Hirano, J. Synchrotron Rad. 5 (1998) 670.
[4] K. Kohra and T. Matsushita, Z. Naturforsch. A 27 (1972) 484.
[5] O. Brümmer, H.R. Höche and J. Nieber, Phys. Status Solidi A 53 (1979) 565.
[6] A. Caticha and S. Caticha-Ellis, Phys. Rev. B 25 (1982) 971; Phys. Status Solidi A 119 (1990) 47.
[7] W. Graeff and G. Materlik, Nucl. Instrum. Methods 195 (1982) 97.
[8] V.I. Kushnir and E.V. Suvorov, JETP Lett. 44 (1986) 262; Phys. Status Solidi A 122 (1990) 391.
[9] J.B. Hastings, D.E. Moncton and Y. Fujii, in: *Proc. of the 1984 Workshop on High Energy Excitations in Condensed Matter*, Los Alamos, NM (1982).
[10] G. Faigel, D.P. Siddons, J.B. Hastings, P.E. Haustein, J.R. Grover, J.P. Remeika and A.S. Cooper, Phys. Rev. Lett. 58 (1987) 2699.
[11] E. Burkel, *Inelastic Scattering of X-rays with Very High Energy Resolution* (Springer, Berlin, 1991).
[12] T. Ishikawa, Y. Yoda, K. Izumi, C.K. Suzuki, X.W. Zhang, M. Ando and S. Kikuta, Rev. Sci. Instrum. 63 (1992) 1015.
[13] T.M. Mooney, T.S. Toellner, W. Sturhahn, E.E. Alp and S.D. Shastri, Nucl. Instrum. Methods A 347 (1994) 348.
[14] A.I. Chumakov, J. Metge, A.Q.R. Baron, H. Grünsteudel, R. Rüffer and T. Ishikawa, Nucl. Instrum. Methods A 383 (1996) 642.
[15] R. Verbeni, F. Sette, M.H. Krisch, U. Bergmann, B. Gorges, C. Halcoussis, K. Martel, C. Masciovecchio, J.F. Ribois, G. Ruocco and H. Sinn, J. Synchrotron Rad. 3 (1996) 62.
[16] T.S. Toellner, M.Y. Hu, W. Sturhahn, K. Quast and E.E. Alp, Appl. Phys. Lett. 71 (1997) 2112.
[17] D.P. Woodruff, D.L. Seymour, C.F. McConville, C.E. Riley, M.D. Crapper, N.P. Prince and R.G. Jones, Phys. Rev. Lett. 58 (1987) 1460.
[18] H. Sinn, A. Bernhard, R. Röhlsberger, J. Sutter and E. Burkel, HASYLAB Jahresbericht (1998).
[19] T. Jach, Y. Zhang, R. Collela, M. de Boissieu, M. Boudard, A.I. Goldman, T.A. Lograsso, D.W. Delaney and S. Kycia, Phys. Rev. Let. 82 (1999) 2904.
[20] V.G. Kohn, I.V. Kohn and E.A. Manykin, JETP 89 (1999) 500.
[21] J. Sutter, E.E. Alp, G. Bortel, M.Y. Hu, P.L. Lee, W. Sturhahn and T.S. Toellner, to be published.
[22] F. Schmid, C.P. Khattak and D.M. Felt, Am. Ceram. Soc. Bull. 73(2) (1994) 39.
[23] A. Kirfel and K. Eichhorn, Acta Crystallogr. A 46 (1990) 271.
[24] P. Aldebert and J.P. Traverse, J. Am. Ceram. Soc. 65 (1982) 460.
[25] A.S. Brown, M.A. Spackman and R.J. Hill, Acta Crystallogr. A 49 (1992) 513.
[26] P. Thompson, D.E. Cox and J.B. Hastings, J. Appl. Cryst. 20 (1987) 79.
[27] J. Lewis, D. Schwarzenbach and H.D. Flack, Acta Crystallogr. A 38 (1982) 733.
[28] W.M. Yim and R.J. Paff, J. Appl. Phys. 45 (1973) 1456.
[29] S. Caticha-Ellis, R. Boyce and H. Winick, Nucl. Instrum. Methods A 291 (1990) 132.

[30] D.E. Moncton, Rev. Sci. Instrum. 67 (1996) 3380.
[31] Yu.V. Shvyd'ko, G.V. Smirnov, S.L. Popov and T. Hertrich, JETP Lett. 53 (1991) 69.
[32] A.Q.R. Baron, Nucl. Instrum. Methods A 352 (1995) 665.
[33] M. Lucht, Diplomarbeit, Universität Hamburg (1998), available from `http://www.rrz.uni-hamburg.de/hfww/publications/diploma.html`.
[34] A. Reisman, M. Berkenblit, J. Cuomo and S.A. Chan, J. Electrochem. Soc. 118 (1971) 1653.
[35] Yu.V. Shvyd'ko, J. Jäschke, M. Lucht, M. Gerken, H.D. Rüter and E. Gerdau, unpublished.
[36] Yu.V. Shvyd'ko, J. Jäschke, M. Lucht, E. Gerdau, M. Gerken, M. Lerche, H.D. Rüter and H.C. Wille, to be published.
[37] Yu.V. Shvyd'ko, M. Lucht, E. Gerdau, E. Alp and J. Sutter, to be published.
[38] Yu.V. Shvyd'ko, M. Gerken, H. Franz, M. Lucht and E. Gerdau, to be published.
[39] I. Koyama, Y. Yoda, X.W. Zhang, M. Ando and S. Kikuta, Japn. J. Appl. Phys. 35 (1996) 6297.
[40] S. Kikuta, Hyp. Interact. 90 (1994) 335.
[41] Yu.V. Shvyd'ko, Phys. Rev. B 59 (1999) 9132; also this issue, section III-1.3.
[42] MOTIF, a program for fitting time spectra of nuclear resonance forward scattering, available from the anonymous `ftp://i2aix04.desy.de/pub/motif/` or from the author via e-mail: `yuri.shvydko@desy.de`.
[43] Yu.V. Shvyd'ko and U. van Bürck, this issue, section IV-2.2.
[44] U. van Bürck, W. Potzel, P. Schindelmann, Yu.V. Shvyd'ko, E. Gerdau, O. Leupold and H.D. Rüter, Phys. Rev. A 139 (2000).
[45] R. Mansouri and R.U. Sexl, Gen. Rel. Grav. 8 (1977) 497, 515 and 809.
[46] M. Born and M. Wolf, *Principles of Optics* (Pergamon Press, Oxford, 1964).
[47] A. Steyerl and K.-A. Steinhauser, Z. Phys. B 34 (1979) 221.
[48] A. Caticha and S. Caticha-Ellis, Phys. Status Solidi A 119 (1990) 643.
[49] A. Caticha, K. Alberty and S. Caticha-Ellis, Rev. Sci. Instrum. 67 (1996) 3380.
[50] V.G. Kohn, Yu.V. Shvyd'ko and E. Gerdau, to appear in Phys. Status Solidi B (2000).
[51] M. von Laue, Ergebn. Exakten Naturwiss. 10 (1931) 133.
[52] W.H. Zachariasen, *Theory of X-Ray Diffraction in Crystals* (Willey, New York, 1945).
[53] B. Batterman and H. Cole, Rev. Mod. Phys. 36 (1964) 681.
[54] Z.G. Pinsker, *Dynamical Scattering of X-rays in Crystals* (Springer, Berlin, 1978).